Cross sections of proton-induced reactions on ^{152}Gd, ^{155}Gd and ^{159}Tb with emphasis on the production of selected Tb radionuclides

G.F. Steyn[a,*], C. Vermeulen[a], F. Szelecsényi[b], Z. Kovács[b], A. Hohn[c], N.P. van der Meulen[d,e], R. Schibli[e], T.N. van der Walt[f]

[a] *iThemba Laboratory for Accelerator Based Sciences, P.O. Box 722, Somerset West, 7129, South Africa*
[b] *Cyclotron Application Department, ATOMKI, P.O. Box 51, H-4001, Debrecen, Hungary*
[c] *Department of Nuclear Medicine, University Medical Centre Rostock, Rostock, Germany*
[d] *Laboratory of Radiochemistry and Environmental Chemistry, Paul Scherrer Institute, 5232 Villigen-PSI, Switzerland*
[e] *Center of Radiopharmaceutical Science, Paul Scherrer Institute, 5232 Villigen-PSI, Switzerland*
[f] *Faculty of Applied Sciences, Cape Peninsula University of Technology, P.O. Box 1906, Bellville, 7535, South Africa*

Abstract

Cross sections are presented for various Dy, Tb and Gd radionuclides produced in the proton bombardment of ^{159}Tb as well as for the reactions ^{152}Gd(p,4n)^{149}Tb and ^{155}Gd(p,4n)^{152}Tb up to 66 MeV. The experimental excitation functions are compared with theoretical predictions by means of the geometry-dependent hybrid (GDH) model as implemented in the code ALICE/ASH, as well as with values from the TENDL-2012 library and previous literature experimental data, where available. Physical yields have been derived for the production of some of the medically important radioterbiums, namely ^{149}Tb (radionuclide therapy), ^{152}Tb (PET) and ^{155}Tb (SPECT). The indirect production of high-purity ^{155}Tb via the decay of its precursor ^{155}Dy is reported. The possibility of a large-scale production facility based on a commercial 70 MeV cyclotron is also discussed.

Keywords:
66 MeV protons, radionuclide production, ^{149}Tb, ^{152}Tb, ^{155}Tb, excitation functions, integral yields

---

1. Introduction

Several members of the radiolanthanides have been studied in recent years for their potential in nuclear medicine. Recently, Müller *et al.* [1] reported on a preclinical study of new tumour-targeting radiopharmaceuticals labeled with a unique quadruplet of Tb radionuclides, namely ^{149}Tb, ^{152}Tb, ^{155}Tb and ^{161}Tb. These radionuclides are unique in that they collectively contain properties suitable for all thee major modalities of nuclear medicine, namely PET, SPECT and radionuclide therapy, from the same element. Müller *et al.* reported excellent results with a folate-based targeting agent containing a DOTA chelator for binding the Tb to the biomolecule. Both ^{152}Tb (PET) and ^{155}Tb (SPECT) imaging of folate receptor (FR)-positive human tumours xenografted into mice were shown to be of high quality. In addition, the same compound labeled with the therapeutic Tb radionuclides (^{149}Tb and ^{161}Tb) demonstrated conclusive results on remission of the disease. While independent studies were performed with the α-particle emitter (^{149}Tb) and the β^- emitter (^{161}Tb), the authors speculated that cocktails of these two isotopes to optimize the efficacy of

---

[*] Corresponding author.
Email address: `deon@tlabs.ac.za` (G.F. Steyn)

the treatment might be an intriguing option, which required further systematic investigation. For further information as well as an account of prior work, the reader is referred to Ref. [1].

The majority of the radioterbiums is not yet generally available. Except for the reactor produced ^{161}Tb, the large-scale production of the other radioterbiums, with a radionuclidic purity suitable for medical use, has not yet been demonstrated. In one of the earlier studies in the literature, Levin *et al.* [2] demonstrated the photonuclear production of ^{155}Tb via the reaction ^{156}Dy(γ,n)^{155}Dy$\rightarrow$^{155}Tb, using bremsstrahlung with a maximum energy of 25 MeV at an electron accelerator. A radionuclidic purity $> 99.9\%$ could be obtained, which is substantially higher than what can be obtained using reactions suitable for a cyclotron. While their electron beam current was rather low and the corresponding yield relatively small, these authors speculated about large-scale production possibilities with future electron accelerators having orders of magnitude higher beam intensities. A number of studies investigated the use of ^{12}C beams. Allen *et al.* [3] and Zaitseva *et al.* [4] studied the ^{nat}Nd(^{12}C,xn)^{152}Dy$\rightarrow$^{152}Tb and ^{nat}Nd(^{12}C,xn)^{149}Dy$\rightarrow$^{149}Tb reactions, respectively. While useful yields could be obtained, the end product inevitable contained a mixture of Tb radionuclides. This is clearly a general problem when charged-particle induced reactions are utilized, even on highly enriched targetry. Electromagnetic (EM) isotope separation is used at the ISOLDE facility of CERN for the collection of radioterbiums produced in proton-induced spallation reactions on Ta [1, 3, 5]. EM separation may yet prove to be the only feasible way to ensure a radionuclidic purity close to 100%. It is interesting to contemplate this form of separation, in conjunction with nuclear reactions at energies low enough to be suitable for commercial cyclotrons, as an option for the large-scale production of radioterbiums in a dedicated facility. Compared to the large scale of ISOLDE, a facility based on a commercial cyclotron would indeed be small and compact.

This present study reports on the work of a collaboration established to measure production cross sections for the direct formation of ^{149,152,155}Tb in ^{152,155}Gd + p as well as for the indirect formation of ^{155}Tb via the decay of its precursor ^{155}Dy in ^{159}Tb + p. Enriched ^{152}Gd and ^{155}Gd target materials were used as well as natural Tb, which is mono-isotopic ^{159}Tb (100%). The new measurements were prompted, in part, by a previous study on proton-induced reactions on ^{nat}Gd [6] up to 66 MeV. This is close to the energy region covered by the new generation of commercial 70 MeV cyclotrons [7] which can deliver beams of high intensity (several hundred μA). A particular aspect of the present investigation is to establish whether a commercial 70 MeV cyclotron will be suitable for the large-scale production of ^{149}Tb, ^{152}Tb and ^{155}Tb.

The relevant part of the nuclide chart is presented in Fig. 1. This a simplified diagram in that many of the shorter-lived metastable states, which feed the respective ground states, have been omitted. Also, the data were taken from the compilation of Firestone and Eckström [8]. The relevant proton-induced nuclear reactions are listed in Table 1. As already discussed in Ref. [6], this part of the nuclide chart is particularly unfriendly (from a radionuclide production point of view) due to seven stable Gd nuclei, which lead to many open reaction channels. In addition, a relatively large number of Tb radionuclides have half-lives in the region of several hours to a few days. Consequently, the production of the medically important Tb radionuclides in a radionuclidically pure form, and not only in a no-carrier-added (NCA) form, is rather compromised. Another complicating factor is that the location of ^{149}Tb is quite far from the line of stability. As will be discussed later, it may yet transpire that EM isotope separation may have to be a compulsory component of a large-scale production facility for these Tb radionuclides.

Cross sections are presented for ^{153,155,157,159}Dy, ^{153,154m2,155,156}Tb and ^{151,153}Gd in ^{159}Tb + p as well as for ^{152}Gd(p,4n)^{149}Tb and ^{155}Gd(p,4n)^{152}Tb. For most of these reactions, no previously measured data could be found in the literature. Physical yields have also been derived for the reactions relevant to ^{149,152,155}Tb production.

2. Experimental

2.1. Irradiations

The well-known stacked-foil technique was employed to measure the excitation functions of radionuclides produced in ^{159}Tb + p from the (p,n) reaction threshold up to 66 MeV. In the case of ^{152}Gd + p and ^{155}Gd + p, only the energy region relevant to the (p,4n) reaction was investigated. Three foil stacks were irradiated in this study, henceforth referred to as Stacks 1, 2 and 3, using 66 MeV proton beams supplied by the separated-sector cyclotron (SSC) facility of iThemba LABS. The foil stacks were bombarded in an accurately calibrated Faraday chamber mounted at the end of an external beam line. This irradiation chamber, based on the design of the RERAME (REcoil RAnge MEasurements) facility of the Laboratory Nazionale del Sud (LNS) in Catania, Italy, has been described in detail elsewhere [9]. The beam was collimated to a spot of 4 mm in diameter. The average beam current was 50 nA and the irradiation time was 2 h for each stack. The beam current and accumulated charge were measured with a Brookhaven Instruments Corporation Model 1000C current integrator. The current and charge values were also logged in 1 second intervals to an analysis computer using the LabVIEW software. The beam energy was accurately measured using a calibrated 90° bending magnet.

Stacks 1 and 2 contained thin targets prepared from oxides of Gd and Tb using the sedimentation technique developed by Rösch *et al.* [10]. Gadolinium trioxide (Gd_2O_3) and tetraterbium heptaoxide (Tb_4O_7) powders were obtained from Isoflex USA and Koch Chemicals Ltd., respectively. Due to limited quantities of the enriched Gd powder, only relatively few targets could be made. In each case, fine powder of the target material was sedimented onto a 26 μm thick Ti backing and covered with a 10 μm thick Al foil. The diameter of a sediment layer was 13 mm, defined by the inner diameter of the sedimentation cells used. The thicknesses of the sediment layers varied between 1.4 and 4.4 mg/cm^2 but nominally 2.5 mg/cm^2 for $^{159}Tb_4O_7$, 4 mg/cm^2 for $^{152}Gd_2O_3$ and 1.5 mg/cm^2 for $^{155}Gd_2O_3$. The thickness of each target sediment and foil was determined accurately by weighing. Stack 1 contained seven ^{152}Gd and seven ^{159}Tb targets while Stack 2 contained seven ^{155}Gd targets, covering the energy region 30–62 MeV. The target foils were interspersed with Cu monitor foils of nominally 108 mg/cm^2 thickness (99.99%, Goodfellow, UK) as well as Cu and Al degrader foils of various thicknesses, as required. Just prior to the bombardment, it was decided to degrade the 66 MeV proton beam by a few MeV to better match the expected energy region of the (p,4n) reaction for both ^{152}Gd + p and ^{155}Gd + p with the assembled energy region of each foil stack. This was done with a single Cu degrader placed at the front of each stack. Irradiations of similar stacks at a beam energy of 30 MeV, to cover the energy region relevant to reactions with lower thresholds, have been planned but have not yet been performed. Consequently, as the data sets for (p,xn) reactions where $x < 4$ are still incomplete, only results for the (p,4n) reactions in ^{152,155}Gd + p are presented at this stage.

Stack 1 had another inherent limitation, namely that the ^{152}Gd targets had an enrichment level of only 30.60%. The content of the other stable Gd isotopes are as follows: ^{154}Gd (9.3%), ^{155}Gd (18.1%), ^{156}Gd (14.8%), ^{157}Gd (8.6 %), ^{158}Gd (11%) and ^{160}Gd (7.6%). Although not ideal, these measurements are nevertheless expected to provide useful information for the important reaction ^{152}Gd(p,4n)^{149}Tb, while the interpretation of several of the other (p,xn) reactions may be rather complicated. Note that the natural abundance of ^{152}Gd is only 0.2%, the reason why ^{149}Tb was not observed in the ^{nat}Gd + p study [6]. An increase of the ^{152}Gd content by more than two orders of magnitude should rectify this. In the case of the ^{155}Gd targets, however, no such complications are expected as the level of enrichment was 99.82%.

The decision to irradiate a third stack containing metallic Tb foils was made later. This was done, in part, as a check on the results from the Tb_4O_7 sediment targets. Results from experiments using the sedimentation technique sometimes show unusually large scatter, which could potentially be a problem in stacked-foil experiments having so few targets as Stacks 1 and 2 in this work. The scatter is thought to be a result of sediment targets being rather fragile, sometimes suffering damage either before or during bombardment. A second reason was that for ^{159}Tb + p, almost no excitation function data could be found in the literature, which made it an interesting study in its own right. Also, because of the delay in the investigation of the lower energy region, it was decided to design Stack 3 to cover the entire energy region down to the threshold of the (p,n) reaction. Normally, we prefer not to degrade the 66 MeV beam so far down due to the increasing energy uncertainty with increasing penetration depth in the stack. On the other hand, the lower energy region for ^{159}Tb + p could always be re-investigated later with a lower energy incident beam (e.g. 30 MeV), should compelling reasons exist to do so. Stack 3 consisted of elemental Tb foils of nominally 18.6 mg/cm^2 thickness (99%, Goodfellow Metals, UK), Cu monitor foils of nominally 45.8 mg/cm^2 (99.9%, Goodfellow, UK) throughout the stack, as well as Ti monitor/degrader foils of nominally 115 mg/cm^2 in the region between 20 and 35 MeV. A selection of Al and Cu foils of various thicknesses were used as degraders.

2.2. Radionuclide assays

After bombardment, the activated foils and sediments were repeatedly assayed by means of standard off-line γ-ray spectrometry. Two calibrated HPGe detectors were used. Above about 120 keV, a coaxial Ge detector with a relative efficiency of 18% and a resolution of 1.8 keV at 1.33 MeV was used. For lower photon energies, in particular the 58 keV γ-ray of ^{159}Dy and the 97 keV γ-ray of ^{153}Gd, a planar Ge detector containing a 10 mm thick crystal and a thin Be window was used. This was done because the planar detector has a higher efficiency and a significantly lower Compton background for these low-energy γ-rays. The photopeak areas were determined by means of the quantitative Canberra Genie 2000 analysis software in conjunction with a Canberra DSA 1000 multi-channel analyser system. The efficiency curves for these detectors were determined by means of standard calibrated γ-ray sources traceable to either the BIPM or NIST.

2.3. Data analysis

The cross sections of the observed activation products were calculated from their measured γ-ray emissions using decay data from the online compilation of Firestone and Eckström [8]. The γ-lines used to identify the nuclides of interest are listed in Table 2. The well-known activation formula (see e.g. [11]) was used and corrections were made for decay losses during and after bombardment as well as during counting.

The accumulated charge was directly measured by means of a calibrated current integrator. Consequently, the cross sections extracted from the Cu and Ti monitor foils served only as a consistency check. The results for the ^{nat}Cu(p,x)^{62}Zn monitor reaction are shown in Fig. 2 for all three stacks, together with the standard excitation function recommended by the IAEA [12]. Only the logged beam currents from the electronic current integrator were used for deriving the experimental cross sections. These measurements reproduce the recommended curve satisfactorily, therefore, there was no need to make any corrections based on the monitor reaction results. A similar quality of agreement was found for the ^{nat}Ti(p,x)^{48}V monitor reaction.

Corrections for beam current losses due to nonelastic nuclear interactions were made according to the prescription and tables of Janni [13]. The average proton energy in each foil or sediment was calculated using the code STACK, which contains the stopping power formulae of Anderson and Ziegler [14]. These stopping powers were checked against the newer compilation of Berger [15] and found to be in excellent agreement. A number of independent checks were also performed using the Monte Carlo code SRIM [16] and found to be consistent with the published stopping power tables.

The total uncertainties in the measured cross sections were obtained by summing all the contributing uncertainties in quadrature and are expressed with a 1σ (68%) confidence level. In addition to statistical uncertainties, a systematic uncertainty was estimated to be about 7%, including the uncertainty in beam current integration (3%), detector efficiency (5%), counting geometry (1%), decay corrections (2%) and foil thickness (3%) [17]. The uncertainty in energy of each measured data point was estimated from the uncertainty in incident beam energy, foil thickness and energy straggling in the stack.

3. Theoretical calculations

In this work, theoretical excitation functions were calculated using the Geometry Dependent Hybrid (GDH) model as implemented in the code ALICE/ASH [18]. The calculations were performed using the recommended values for the input parameters according to the comments in the preamble to the code. Level densities were calculated according to the generalized superfluid model (GSM). The normal pairing shift was selected. Experimental nuclidic masses were used where available, else calculated using the built-in Myers and Swiatecki mass formula of the code. A level density parameter of $a = A/9$ and an initial energy bin size of 0.5 MeV were used. The calculations were performed within the frame of the GDH model for the pre-equilibrium emission of protons and neutrons. The subsequent evaporation during the equilibrium stage was calculated according to the Weiskopf-Ewing formalism as implemented in the code. The evaporated particles included protons, neutrons, deuterons and α-particles.

To avoid the known scatter in the high energy “tail” regions of some of the excitation functions, especially in the case of the (p,n) reactions, we adopted the practice of performing sets of calculations, varying the energy bin size (parameter *ED* in the code) from 0.4 to 0.6 MeV in steps of 0.01 MeV, followed by taking the arithmetic average over all sets. This has been reported on extensively in a previous paper [19]. In cases where the scatter was not problematic, an energy bin size of 0.5 MeV was adopted.

In addition to the ALICE/ASH predictions, the measured excitation functions are also compared with the relevant cross sections compiled in the TENDL-2012 library [20, 21].

4. Results and Discussion

The results from Stacks 1 and 2 (i.e. the ^{152}Gd$_2$O$_3$, ^{155}Gd$_2$O$_3$ and ^{159}Tb$_4$O$_7$ sediment targets) are presented in Table 3. The results from Stack 3 (i.e. the Tb metal foils) are presented in Tables 4, 5 and 6. The excitation functions are shown in Figs. 3 though 14 and the derived physical yield curves and other related quantities (e.g. radionuclidic purity) in Figs. 15 through 18.

4.1. The ^{152}Gd(p,4n)^{149}Tb reaction

Because the ^{152}Gd$_2$O$_3$ targets only had a 30.6% level of enrichment of ^{152}Gd, several other reactions also contributed to the direct formation of ^{149}Tb, such as ^{154}Gd(p,6n)^{149}Tb (Q = -43.36 MeV) and ^{155}Gd(p,7n)^{149}Tb (Q = -49.80 MeV). The ^{152}Gd(p,4n)^{149}Tb (Q = -28.21 MeV) reaction, however, is expected to dominate the excitation function. The measured data are shown in Fig. 3, scaled for targets of 100% enrichment. Comparisons are made with ALICE/ASH predictions for the (p,4n) reaction on its own, as well as the sum of the contributions from the (p,4n), (p,6n) and (p,7n) reactions mentioned above, weighed according to the relative ^{152}Gd, ^{154}Gd and ^{155}Gd abundances in the target material, respectively. The ALICE/ASH predictions overestimate the cross sections considerably and have been renormalized (with a scale factor of SF = 0.31) for purposes of comparison with the experimental data. One can clearly see in the figure that both ALICE/ASH curves reproduce the shape of the excitation function quite well, even though the data points are rather few. The excitation function peaks at about 250 mb at an energy of 42 MeV. Also, the contributions from the (p,6n) and (p,7n) reactions are indeed small and feature only at energies above about 55 MeV. Figure 3 also shows the TENDL-2012 values for the (p,4n) reaction which are substantially larger than the measured values and have been renormalized to the measured data for purposes of comparison (scale factor *SF* = 0.39). The TENDL-2012 data do not reproduce the shape of the experimental excitation function nearly as well as the ALICE/ASH predictions and appear to be shifted towards lower energies by about 4–5 MeV.

4.2. The ^{155}Gd(p,4n)^{152}Tb reaction

Concerning the measurements, only the (p,4n) reaction on ^{155}Gd contributed significantly to ^{152}Tb formation as the ^{155}Gd enrichment level was close to 100%. The experimental cross sections are shown in Fig. 4, together with ALICE/ASH predictions and the relevant TENDL-2012 values. The ALICE/ASH and TENDL-2012 values both underestimate the excitation function and have therefore been renormalized to the measurements for purposes of comparison (scale factors *SF* = 1.7 and *SF* = 1.3, respectively). Both predictions are somewhat shifted relative to the measurements – TENDL-2012 towards lower energies and ALICE/ASH towards higher energies. The spline fit through the measured data was used for calculating the integral yield curve, which will be presented later. The excitation function reaches a maximum of about 900 mb at energy of about 39 MeV.

4.3. The ^{159}Tb(p,7n)^{153}Dy reaction

The ^{159}Tb(p,7n)^{153}Dy (Q = -49.6 MeV) reaction could only be observed in three of the Tb metal foils of Stack 3, at the highest energies, as shown in Fig. 5. It is presented here for completeness only. Both ALICE/ASH and TENDL-2012 do not reproduce the onset of the excitation function in the threshold region very well, therefore, a spline fit through the measured data, extrapolated to 70 MeV, has been used to calculate the physical yield curve. This will be further discussed later.

4.4. The ^{159}Tb(p,5n)^{155}Dy reaction

In the case of the ^{159}Tb(p,5n)^{155}Dy (Q = -33.45 MeV) reaction, both the ALICE/ASH prediction, the TENDL-2012 data and the experimental data agree reasonably well in magnitude at the maximum of the excitation function. However, as shown in Fig. 6, the TENDL-2012 results seem to be systematically shifted towards lower energies, while the ALICE/ASH prediction is shifted towards higher energies. There is also good agreement in shape between the ALICE/ASH prediction and the measurements, the main difference being the approximately 2 MeV shift. In contrast, the TENDL-2012 excitation function shows a significantly narrower width in the peak region. While not perfect, the overall agreement between the measurements from Stacks 1 and 3 is acceptable – the majority of the experimental points from the two data sets agree within the experimental uncertainties. This is very reassuring. The excitation function reaches a maximum of about 520 mb at 48 MeV. As before, a spline fit through the measured data, shown in the figure, was used for calculating integral yields.

4.5. The ^{159}Tb(p,3n)^{157}Dy reaction

The results for the ^{159}Tb(p,3n)^{157}Dy (Q = -17.04 MeV) reaction are shown in Fig. 7. The agreement with the ALICE/ASH prediction is very satisfactory, both in absolute magnitude and in shape (the theoretical maximum only slightly higher), while the TENDL-2012 values are somewhat lower with the peak position shifted towards the lower energy side by about 4 MeV. The overall agreement between the measurements from Stacks 1 and 3 is also acceptable. The excitation function reaches a maximum of 1040 mb at about 27 MeV.

4.6. The ^{159}Tb(p,n)^{159}Dy reaction

Figure 8 shows the results for the ^{159}Tb(p,n)^{159}Dy (Q = -1.148 MeV) reaction. The excitation function peaks just over 100 mb at an energy of about 10.4 MeV. The agreement with the only set of previously published data found in the literature, by Hassan *et al.* [22], is reasonable. The ALICE/ASH calculations and TENDL-2012 values largely overpredict the excitation function, however, ALICE/ASH reproduces the peak region quite well when the values are scaled with a factor SF = 0.42. We also noted a strange anomaly in the (p,n) data of TENDL-2012 for a range of target nuclei. There is a notable but spurious second local maximum towards higher energies, which is not characteristic of (p,n) reactions. Previous versions of TENDL also show this anomaly (see Fig. 8). We checked the TENDL data of the (p,n) reaction for many lighter and heavier nuclei as well. The anomaly is notably present for the majority of nuclei between Eu and Bi but seems to be absent below Z = 61. In fact, for some nuclei between Eu and Bi the TENDL-2012 values show a prominent second peak.

4.7. The ^{159}Tb(p,X)^{153}Tb process

Several reaction channels are open for the formation of ^{153}Tb ($T_{1/2}$ = 2.3 d) e.g. ^{159}Tb(p,p6n)^{153}Tb (Q = -46.65 MeV), ^{159}Tb(p,d5n)^{153}Tb (Q = -44.42 MeV), ^{159}Tb(p,t4n)^{153}Tb (Q = -38.16 MeV) as well as indirectly via the the decay of the precursor ^{153}Dy ($T_{1/2}$ = 6.4 h). The measurements were performed after the complete decay of the shorter-lived precursor and the resulting cross sections are therefore cumulative. The measurements are presented in Fig. 9, as well as the ALICE/ASH and TENDL-2012 predictions. It is impossible to make a judgment on the quality of the theoretical predictions as the measurements reflect only the steep slope near an effective threshold somewhat above 50 MeV. It seems, however, as if the TENDL-2012 values are shifted towards lower energies and the ALICE/ASH values towards higher energies. Neither curves can be successfully scaled to the data, therefore, the scale factors were kept at a value of SF = 1. This may be an indication that energy shifts are more likely than over- and underpredictions.

4.8. The ^{159}Tb(p,X)^{154m2}Tb process

Similar to the results of the ^{nat}Gd + p [6], it was only possible to extract cross sections for the m2 state in ^{154}Tb. Both the ALICE/ASH and TENDL-2012 curves had to be scaled considerably for purposes of making a comparison with the measurements (SF = 0.075), as shown in Fig. 10. In this particular case, the cross sections are for the direct production of ^{154m2}Tb due to the very long half-life of the precursor, ^{154}Dy ($T_{1/2}$ = 3×10^6 y). Even though the relevant reaction Q-values are all below 40 MeV (^{159}Tb(p,p5n)^{154m2}Tb, Q = -39.93 MeV; ^{159}Tb(p,d4n)^{154m2}Tb, Q = -37.51 MeV; ^{159}Tb(p,t3n)^{154m2}Tb, Q = -31.25 MeV) no ^{154m2}Tb were detected below 53 MeV. It is difficult to make a conclusive judgement about the agreement between the experimental measurements and the theoretical predictions. It seems, however, that the TENDL-2012 values reproduce the shape of the excitation function better in this case, albeit with an order of magnitude overprediction.

4.9. The ^{159}Tb(p,X)^{155}Tb process

The excitation function of ^{155}Tb ($T_{1/2}$ = 5.42 d) contains contributions which are directly produced (^{159}Tb(p,p4n)^{155}Tb, Q = -30.57 MeV; ^{159}Tb(p,d3n)^{155}Tb, Q = -28.34 MeV; ^{159}Tb(p,t2n)^{155}Tb, Q = -22.09 MeV) as well as an indirectly produced contribution via the decay of a shorter-lived precursor, ^{155}Dy ($T_{1/2}$ = 9.9 h). These measurements were performed after the decay of the precursor, thus, the resulting cross sections are cumulative. As shown in Fig. 4.11, the data span several orders of magnitude and are therefore plotted on a log scale. The agreement with the ALICE/ASH prediction is satisfactory, both in shape and absolute magnitude, although the theoretical values are shifted towards higher energies by about

2 MeV. In contrast, the TENDL-2012 values are shifted somewhat towards lower energies and underestimate the maximum cross section. The excitation function peaks at a value of about 670 mb at 51 MeV.

4.10. The ^{159}Tb(p,X)^{156}Tb process

Two relatively long-lived metastable states, ^{156m1}Tb ($T_{1/2}$ = 1.02 d) and ^{156m2}Tb ($T_{1/2}$ = 5 h), both decay to the ground state of ^{156}Tb ($T_{1/2}$ = 5.4 d). The measurements were performed after the near-complete decay of the metastable states. There is no Dy precursor (^{156}Dy is stable). The experimental results are shown in Fig. 12, together with the ALICE/ASH calculations and the TENDL-2012 values. The TENDL-2012 results are in excellent agreement with the measured data. The ALICE/ASH prediction seems to start at a too-high threshold and also slightly overpredicts the excitation function maximum.

4.11. The ^{159}Tb(p,X)^{151}Gd process

Only a few values could be measured above 50 MeV, dominated by the ^{159}Tb(p,α5n)^{151}Gd (Q = -30.84 MeV) reaction as the ^{159}Tb(p,2p7n)^{151}Gd (Q = -59.89 MeV) is not contributing significantly in this energy region. The results are shown in Fig. 13. The ALICE/ASH prediction is reasonable while the TENDL-2012 values are shifted towards lower energies.

4.12. The ^{159}Tb(p,X)^{153}Gd process

The contributions from both the ^{159}Tb(p,α3n)^{153}Gd (Q = -15.99 MeV) and ^{159}Tb(p,2p5n)^{153}Gd (Q = -44.30 MeV) reactions are clearly visible, as shown in Fig. 14. The sharp rise starting just below 60 MeV is from the latter reaction, which is not well reproduced by the ALICE/ASH predictions, nor by TENDL-2012. This kind of behaviour in an excitation function is not unusual and has been described before, e.g. for the ^{68}Zn(p,X)^{64}Cu reaction, where the contributions from the ^{68}Zn(p,αn)^{64}Cu and the ^{68}Zn(2p,3n)^{64}Cu reactions show a similar trend [9].

4.13. Integral yield calculations

Thick target yields for ^{149}Tb and ^{152}Tb, derived from the excitation functions for the ^{152}Gd(p,4n)^{149}Tb and ^{155}Gd(p,4n)^{152}Tb reactions, respectively, are shown in Fig. 15. Note that these are *physical yields*. In the case of ^{149}Tb, the scaled ALICE/ASH prediction shown in Fig. 3 (solid curve) was used for this purpose, while the spline fit in Fig. 4 was used for ^{152}Tb. With an energy window of 66 MeV down to threshold (about 30 MeV), a physical yield of 2556 MBq/μAh (69.1 mCi/μAh) can be expected for ^{149}Tb and 1924 MBq/μAh (52.0 mCi/μAh) for ^{152}Tb from the above (p,4n) reactions, respectively. These are very high yields but, unfortunately, do not lead to radionuclidically pure products, as already mentioned. The value for ^{152}Tb is higher than the rather conservative estimate of 1200 MBq/μAh (32.4 mCi/μAh) from the ^{nat}Gd + p study [6].

Thick target yields for ^{153,155,157,159}Dy in ^{159}Tb +p, derived from spline fits through the measured excitation function data (see Figs. 5–8) are shown in Fig. 16. It is evident that the ^{155}Tb produced via ^{155}Dy decay will contain the decay products of a considerable amount of ^{157}Dy as well, in any energy window. However, ^{157}Tb is long-lived with a half-life of 71 y [8], therefore only low levels of ^{157}Tb activity are to be expected in the final product. The yield of ^{159}Dy is quite low as it is also quite long-lived ($T_{1/2}$ = 144.4 d) and furthermore it decays to stable ^{159}Tb, thus, it is no contributor to any radiocontaminant. Nevertheless, stable Tb will affect labeling efficiency, which should be taken into consideration. Lastly, ^{153}Dy will contribute ^{153}Tb as a radiocontaminant but only above 59 MeV.

To produce ^{155}Tb via ^{155}Dy decay would require two chemical separations. The Dy should be separated from the Tb target material as soon as possible after the end of bombardment (EOB). An optimum waiting time would then be required to allow for maximum growth of ^{155}Tb, followed by a second chemical separation to isolate the Tb from the remaining Dy. In order to evaluate this production route, one needs to investigate the growth and decay characteristics of all the relevant Dy radionuclides on a common timeline. It is also necessary to make some assumptions on the duration of the chemical separations. Let $t = 0$ be the time when an isolated quantity of pure ^{155}Dy starts to decay. The growth and decay curve of ^{155}Tb formed via the decay of the ^{155}Dy is shown in Fig. 17, where $A_d(t)$ denotes the activity of the daughter at time t and $A_m(0)$ denotes the activity of the mother radionuclide at time $t = 0$. The curve reaches a maximum at $t = 39.6$ h, which should be close to the optimum waiting time after the first chemical separation before performing the second chemical separation, depending on the effective duration of the separation procedure. The dashed line in Fig. 17 shows the points in time where the ^{155}Tb activity reaches 90% of the maximum. These times are $t = 21.6$ h and $t = 72.5$ h during the periods of net growth and net decay, respectively. This is rather convenient, as it indicates that there is an interval of many hours during which the second chemical separation can be performed. A FORTRAN code developed previously [23] was adapted to follow the growth and decay of all the produced Dy radionuclides on a common timeline, taking the durations of chemical separations into account. In fact, the bombardment time, waiting times and processing times are all variables. Different production scenarios can therefore be investigated. The code calculates the yield and radionuclidic purity as well as the ^{155}Tb purity as a percentage of all Tb nuclei produced.

As an example of the kind of results one can obtain, the conditions of Table 7, which we consider to be realistic, will be used in the following calculations. A bombardment time of 10 h is just over one half-life of the mother radionuclide, ^{155}Dy. Waiting time 1 is the time interval between EOB and the start of the first chemical separation and includes tasks such as the removal of the target from the beamline, transport to a reception hot cell, decapsulation and transfer of the irradiated material to a processing hot cell. The actual ion-exchange procedure of the chemical separations is assumed to have a duration of 1 h each. Waiting time 2 is the period required for the accumulation of ^{155}Tb from ^{155}Dy decay and is taken as 39 h. Waiting time 3 is a short period between the end of the second chemical separation and the reference time, allowing for the removal of the product from the hot cell and performing a measurement of the activity. The exit energy of the energy window is taken as 35 MeV and the entrance energy is varied between 50 and 70 MeV. The results are shown in Fig. 18, plotted versus the entrance proton energy. The yield rises from 39.8 GBq (1074 mCi) at an incident energy of 50 MeV to 116.6 GBq (3151 mCi) at an incident energy of 70 MeV. It is evident that this production route is suitable for the production of Ci quantities of ^{155}Tb. The radionuclidic purity is better than 99.9% at all incident energies below 60 MeV but decreases monotonically above 60 MeV to a value of about 88% at 70 MeV. The number of ^{155}Tb nuclei, expressed as a percentage of all produced Tb nuclei, has a value of 57.5% at 40 MeV, increasing towards higher energies until reaching a maximum of 68.1% at 62 MeV, then decreases slightly to a value of 65.4% at 70 MeV.

It is evident that this indirect production route can provide high yields of ^{155}Tb with excellent radionuclidic purity, however, nuclei of other stable and long-lived Tb species are also produced. This reduces the purity in terms of the fraction of all Tb nuclei produced, which may affect the labeling efficiency.

5. Electromagnetic Isotope Separation

Electromagnetic (EM) isotope separation (also called EM mass separation) may be the only method to obtain highly radionuclidically pure ^{149}Tb. In principle, the ^{152}Gd(p,n)^{152}Tb and ^{155}Gd(p,n)^{155}Tb reactions can provide high purity ^{152}Tb and ^{155}Tb, respectively, provided that target material with a sufficiently high level of enrichment (close to 100%) are used. EM isotope separation will, however, be required if the respective high-yield (p,4n) reactions are utilized. In fact, it might be possible to collect sufficient quantities of pure ^{152}Tb and ^{155}Tb simultaneously with the ^{149}Tb, depending on the chosen target material. It is, therefore, interesting to contemplate the possibility of using EM isotope separation as the technology of choice to remove isotopic impurities. Recently, Lapi *et al.* [24] and D'Auria *et al.* [25] demonstrated efficient EM isotope separation for ^{99}Mo. These authors also speculated about using EM isotope separation for many other medically important radionuclides, some of which can be produced in sufficient quantities via reactions such (n,γ) and (γ,n) but which result in products with a low specific activity. While the principles of EM isotope separation are well known for many decades, practical issues remain, e.g. ion source reliability and efficiency as well as the challenges associated with handling high levels of radioactivity after extensive operation at high beam intensities.

It is the belief of the majority of the present authors that should ^{149}Tb prove to be important enough to nuclear medicine at some time in the future, the present engineering problems, which preclude large-scale productions with good radionuclidic purity, will be solved. This happened before, e.g. in the case of ^{18}F. Furthermore, future dedicated facilities may be small and compact, in stark contrast to the large spallation + ISOL facilities such as ISOLDE at CERN. A possible scenario may include a commercial 70 MeV cyclotron, such as the IBA Cyclone 70 XP, Best BSCI 70p or CIAE CYCCIAE70 [7] in conjunction with a compact EM isotope separator, such as that of the Ion Source Test Facility (ISTF) at TRIUMF [25]. This last-mentioned facility is a fantastic step in the right direction and may be ideally suited for proof-of-principle studies. In fact, prior chemical processing of batch targets may provide feedstock of already relatively high specific activity for the EM separator system, which will then provide the final purifying step.

6. Conclusion

Measured cross sections for the ^{152}Gd(p,4n)^{149}Tb, ^{155}Gd(p,4n)^{152}Tb and ^{159}Tb(p,xn)^{153,155,157,159}Dy reactions have been presented. In the case of ^{159}Tb + p, cross sections for various Tb and Gd radionuclides have also been extracted, some directly produced and others cumulatively. Integral yields for ^{149}Tb and ^{152}Tb in the proton bombardment of enriched Gd targets have been calculated, as well as the yield and purity to be expected from the indirect production route ^{159}Tb(p,5n)^{155}Dy$\rightarrow^{155}$Tb. It is shown that excellent yields can readily be obtained with a commercial 70 MeV cyclotron, however, EM isotope separation may be the only way to achieve ^{149,152,155}Tb products with a high level of radionuclidic purity and the desired specific activity. Furthermore, it is speculated that dedicated, compact facilities for their production may be feasible. However, this would require a great deal of further experimental investigation and development work. A facility such as the ISTF at TRIUMF may be ideally suited to pursue such studies.

Concerning nuclear data needs, a consistent experimental investigation of the ^{152}Gd(p,n)^{152}Tb and ^{155}Gd(p,n)^{155}Tb reactions is still lacking. This will require ^{152}Gd + p and ^{155}Gd + p stacked-foil experiments in the energy region from the respective (p,n) reaction thresholds up to about 30 MeV.

Acknowledgements

This work is based on the research supported in part by the National Research Foundation of South Africa (Grant specific unique reference number (UID) 85507). The Grantholder acknowledges that opinions, findings and conclusions or recommendations expressed in any publication generated with the NRF supported research are that of the authors, and that the NRF accepts no liability whatsoever in this regard.

References

[1] C. Müller, K. Zhernosekov, U. Köster, K. Johnston, A. Hohn, T. N. van der Walt, A. Türler, R. Schibli, A unique matched quadruplet of terbium radioisotopes for PET and SPECT and for α- and β^--radionuclide therapy: An in vivo proof-of-concept study with a new receptor-targeted folate derivative, J. Nucl. Med. 53 (2012) 1951–1959.

[2] V. I. Levin, A. B. Malanin, I. N. Tronova, Production of radionuclides by photonuclear reactions. I. Production of terbium-155 and thulium-167 using the electron accelerator EA-25, Radiochem. Radioanal. Lett. 49 (1981) 111-118.

[3] B. J. Allen, G. Goozee, S. Sarkar, G. Beyer, C. Morel, A. P. Byrne, Production of terbium-152 by heavy ion reactions and proton induced spallation, Appl. Radiat. Isot. 54 (2001) 53–58.

[4] N. G. Zaitseva, S. N. Dmitriev, O. D. Maslov, L. G. Molokanova, G. Ya. Starodub, S. V. Shishkin, T. V. Shishkina, G. J. Beyer, Terbium-149 for nuclear medicine. The production of ^{149}Tb via heavy ions induced nuclear reactions. Czech. J. Phys. 53 (2003) A455–A458.

[5] G. J. Beyer, M. Miederer, S. Vranješ-Durić, J. J. Čomor, G. Künzi, O. Hartley, R. Senekowitsch-Schmidtke, D. Soloviev, F. Buchegger, Targeted alpha therapy in vivo: direct evidence for single cancer cell kill using ^{149}Tb-rituximab, Eur. J. Nucl. Med. Biol. Imaging 31 (2004) 547–554.

[6] C. Vermeulen, G. F. Steyn, F. Szelecsényi, Z. Kovács, K. Suzuki, K. Nagatsu, A. Hohn, T. N. van der Walt, Cross sections of proton-induced reactions on ^{nat}Gd with special emphasis on the production possibilities of ^{152}Tb and ^{155}Tb, Nucl. Instr. and Meth. B 275 (2012) 24–32.

[7] P. Schmor, Review of cyclotrons for the production of radioactive isotopes for medical and industrial applications. Rev. Accl. Sci. Tech. 4 (2011) 103–116.

[8] R. B. Firestone, L. P. Eckström, WWW Table of Radioactive Isotopes, Version 2.1, January 2004. Available from URL: http://ie.lbl.gov/toi.

[9] F. Szelecsényi, G. F. Steyn, Z. Kovácz, C. Vermeulen, N. P. van der Meulen, S. G. Dolley, T. N. van der Walt, K. Suzuki, K. Mukai, Investigation of the ^{66}Zn(p,2pn)^{64}Cu and ^{68}Zn(p,x)^{64}Cu nuclear processes up to 100 MeV: Production of ^{66}Cu. Nucl. Instr. and Meth. B 240 (2005) 625–637.

[10] F. Rösch, S. M. Qaim, G. Stöcklin, Nuclear data relevant to the production of the positron emitting radioisotope ^{86}Y via the ^{86}Sr(p,n) and ^{nat}Rb(^{3}He,xn)-processes. Radiochim. Acta 61 (1993) 1–8.

[11] G. R. Gilmore, Practical Gamma-ray Spectrometry, 2nd Edition. John Wiley & Sons, Est Sussex, England, 2008, p. 20.

[12] K. Gul, A. Hermanne, M. G. Mustafa, F. M. Nortier, P. Obložinský, S. M. Qaim, B. Scholten, Y. Shubin, S. Takács, F. T. Tárkányi and Z. Zhuang, Charged particle cross-section database for medical radioisotope production: diagnostic radioisotopes and monitor reactions. IAEA-TECDOC-1211, IAEA, Vienna, May 2001. Available from URL: http://www-nds.iaea.org/medical/. (last updated 2005).

[13] J. F. Janni, Proton range-energy tables: Part 1. At. Data Nucl. Data Tables 27 (1982) 142–339. Proton range-energy tables: Part 2. At. Data Nucl. Data Tables 27 (1982) 341–529.

[14] H. H. Anderson, J. F. Ziegler, Hydrogen stopping powers and ranges in all elements. In: The Stopping and Ranges of Ions in Matter, Vol. 3 (Ed. J. F. Ziegler), Pergamon, New York, 1977, p. 1.

[15] M. J. Berger, J. S. Coursey, M. A. Zucker, J. Chang, Stopping-Power and Range Tables for Electrons, Protons and Helium Ions. Last update, August 2004. Available from URL: http://physics.nist.gov/Star.

[16] J. F. Ziegler, J. P. Biersack, The Stopping and Range of Ions in Matter (SRIM-2006) version 2006.01. Available from URL: http://www.srim.org/.

[17] Guide to the expression of uncertainty in measurements. International Organization for Standardization (ISO), Geneva, ISBN 92-67-10188-9, 1995.

[18] C. H. M. Broeders, A. Yu. Konobeyev, Yu. A. Korovin, V. P. Lunev, M. Blann, ALICE/ASH - Pre-compound and Evaporation Model Code System for Calculation of Excitation Functions, Energy and Angular Distributions of Emitted Particles in Nuclear Reactions at Intermediate Energies. Wissenschaftliche Berichte FZKA 7183, Forschungszentrum Karlsruhe, 2006.

[19] F. Szelecsényi, C. Vermeulen, G. F. Steyn, Z. Kovács, K. Aardaneh, T. N. van der Walt, Excitation functions of ^{186,187,188,189,190,192}Ir formed in proton-induced reactions on highly enriched ^{192}Os up to 66 MeV. Nucl. Instr. and Meth. B 268 (2010) 3306–3314.

[20] A. J. Koning, D. Rochman, Modern nuclear data evaluation with the TALYS code system. Nuclear Data Sheets 113 (2012) 2841–2934.

[21] A. J. Koning, D. Rochman, S. van der Marck, J. Kopecky, J. Ch. Sublet, S. Pomp, H. Sjöstrand, R. Forrest, E. Bauge, H. Henriksson, TENDL-2012: TALYS-based evaluated nuclear data library, version 5. Released on 11 January 2013. Available from URL: http://www.talys.eu/tendl-2012.html.

[22] H. E. Hassan, F. S. Al-Saleh, K. F. Hassan, A. Sayed, Z. A. Saleh, Proton induced reactions on Tb-159 and La-139 for producing Dy-159 and Ce-139, In: Proc. 6th Int. Conf. on Nuclear and Particle Physics (2007, Luxor, Egypt, Ed. M. N. H. Comsan), p. 209–217.

[23] G. F. Steyn, C. Vermeulen, F. M. Nortier, F. Szelecsényi, Z. Kovácz, S. M. Qaim, Production of no-carrier-added ^{139}Pr via precursor decay in the proton bombardment of ^{nat}Pr. Nucl. Instr. and Meth. B 252 (2006) 149–159.

[24] S. E. Lapi, K. Ladouceur, T. J. Ruth, J. M. D'Auria, The MORE Project: An alternative route to the production of high specific activity ^{99}Mo, In: Proc. Int. Symp. on Technetium and Other Radiometals in Chemistry and Medicine (Terachem 2010, Bressanone, Bolzano, Italy, Ed. U. Mazzi), SG Editoriali, Padova, 2010, p. 435–436.

[25] J. M. D'Auria, R. Keller, K. Ladouceur, S. E. Lapi, T. J. Ruth, P. Schmor, An alternate approach to the production of radioisotopes for nuclear medicine applications. Rev. Sci. Instr. 84 (2013) 034705-1 – 034705-4.

Table 1: Proton-induced reactions for the relevant Tb, Dy and Gd radionuclides.

Reaction	Q value (MeV)	Natural Isotopic Abundance[a]	Reaction	Q value (MeV)
^{152}Gd(p,4n)^{149}Tb	-28.21	0.20%	^{159}Tb(p,n)^{159}Dy	-1.148
^{154}Gd(p,6n)^{149}Tb	-43.36	2.18%	^{159}Tb(p,3n)^{157}Dy	-17.04
^{155}Gd(p,7n)^{149}Tb	-49.80	14.80%	^{159}Tb(p,5n)^{155}Dy	-33.45
^{156}Gd(p,8n)^{149}Tb	-58.33	20.47%	^{159}Tb(p,7n)^{153}Dy	-49.60
^{152}Gd(p,n)^{152}Tb	-4.77	0.20%	^{159}Tb(p,p3n)^{156}Tb	-23.66
^{154}Gd(p,3n)^{152}Tb	-19.91	2.18%	^{159}Tb(p,d2n)^{156}Tb	-21.43
^{155}Gd(p,4n)^{152}Tb	-26.35	14.80%	^{159}Tb(p,tn)^{156}Tb	-15.17
^{156}Gd(p,5n)^{152}Tb	-34.89	20.47%	^{159}Tb(p,p4n)^{155}Tb	-30.57
^{157}Gd(p,6n)^{152}Tb	-41.25	15.65%	^{159}Tb(p,d3n)^{155}Tb	-28.34
^{158}Gd(p,7n)^{152}Tb	-49.18	24.84%	^{159}Tb(p,t2n)^{155}Tb	-22.09
^{160}Gd(p,9n)^{152}Tb	-62.58	21.86%	^{159}Tb(p,p5n)^{154m2}Tb	-39.73
^{154}Gd(p,γ)^{155}Tb	4.83	2.18%	^{159}Tb(p,d4n)^{154m2}Tb	-37.51
^{155}Gd(p,n)^{155}Tb	-1.61	14.80%	^{159}Tb(p,t3n)^{154m2}Tb	-31.25
^{156}Gd(p,2n)^{155}Tb	-10.14	20.47%	^{159}Tb(p,p6n)^{153}Tb	-46.65
^{157}Gd(p,3n)^{155}Tb	-16.50	15.65%	^{159}Tb(p,d5n)^{153}Tb	-44.42
^{158}Gd(p,4n)^{155}Tb	-24.44	24.84%	^{159}Tb(p,t4n)^{153}Tb	-38.16
^{160}Gd(p,6n)^{155}Tb	-37.83	21.86%	^{159}Tb(p,α3n)^{153}Gd	-15.99
^{160}Gd(p,γ)^{161}Tb	6.81	21.86%	^{159}Tb(p,2p5n)^{153}Gd	-44.30
			^{159}Tb(p,α5n)^{151}Gd	-30.84
			^{159}Tb(p,2p7n)^{151}Gd	-59.89

[a] Taken from Firestone & Eckström [8].

Table 2: Investigated Tb, Dy and Gd radionuclides and their decay properties used for experimental cross-section determinations[a].

Nuclide	Half-life	Decay mode	γ-rays (keV)	Intensity (%)
^{149}Tb	4.118 h	$\epsilon+\beta^+$: 83.3% α: 16.7%	352.24	29.43
^{152}Tb	17.5 h	$\epsilon+\beta^+$: 100% β^+: 17%	271.13 344.27 586.26	8.6 65.0 9.4
^{153}Tb	2.3 d	$\epsilon+\beta^+$: 100%	212.00	31.0
^{154m2}Tb	22.7 h	$\epsilon+\beta^+$: 98.2% IT: 1.8%	225.94	26.8
^{155}Tb	5.32 d	ϵ: 100%	180.10 367.23	7.45 1.48
^{156}Tb	5.35 d	$\epsilon+\beta^+$: 100%	199.21 356.42 534.32	40.9 13.6 66.6
^{153}Dy	6.4 h	$\epsilon+\beta^+$: 99.99%	213.75	10.9
^{155}Dy	9.9 h	$\epsilon+\beta^+$: 100%	226.92	68.4
^{157}Dy	8.14 h	$\epsilon+\beta^+$: 100%	326.16	92.0
^{159}Dy	144.4 d	ϵ: 100%	58.00	2.22
^{151}Gd	124.0 d	ϵ: 100%	153.60 243.28	6.20 5.60
^{153}Gd	240.4 d	ϵ: 100%	97.43 103.18	29.0 21.1

[a] Taken from Firestone & Eckström [8].

Table 3: Measured cross sections for the production of Tb and Dy radionuclides in the irradiation of ^{152,155}Gd and ^{nat}Tb with protons – results from Stacks 1 and 2.

Proton energy (MeV)	Cross section (mb)			
	^{152}Gd(p,4n)^{149}Tb	^{155}Gd(p,4n)^{152}Tb	^{159}Tb(p,5n)^{155}Dy	^{159}Tb(p,3n)^{157}Dy
31.73 ± 1.11	–	$(2.24 \pm 0.21) \times 10^{+2}$	–	–
35.69 ± 0.98	–	–	–	$(3.73 \pm 0.34) \times 10^{+2}$
35.52 ± 0.99	$(1.71 \pm 0.19) \times 10^{+2}$	–	–	–
36.71 ± 0.96	–	$(8.04 \pm 0.74) \times 10^{+2}$	–	–
41.31 ± 0.84	$(2.48 \pm 0.27) \times 10^{+2}$	–	–	–
41.46 ± 0.83	–	–	$(1.80 \pm 0.17) \times 10^{+2}$	$(2.03 \pm 0.19) \times 10^{+2}$
42.22 ± 0.82	–	$(8.21 \pm 0.75) \times 10^{+2}$	–	–
46.55 ± 0.71	$(1.63 \pm 0.19) \times 10^{+2}$	–	–	–
46.69 ± 0.71	–	–	$(5.07 \pm 0.47) \times 10^{+2}$	$(1.33 \pm 0.12) \times 10^{+2}$
47.25 ± 0.70	–	$(3.77 \pm 0.35) \times 10^{+2}$	–	–
52.25 ± 0.58	$(9.43 \pm 1.28) \times 10^{+1}$	–	–	–
52.38 ± 0.58	–	–	$(5.52 \pm 0.51) \times 10^{+2}$	$(1.12 \pm 0.10) \times 10^{+2}$
52.76 ± 0.57	–	$(2.33 \pm 0.21) \times 10^{+2}$	–	–
57.52 ± 0.48	$(5.92 \pm 0.88) \times 10^{+1}$	–	–	–
57.64 ± 0.48	–	–	$(4.16 \pm 0.38) \times 10^{+2}$	$(1.05 \pm 0.10) \times 10^{+2}$
57.87 ± 0.47	–	$(1.63 \pm 0.15) \times 10^{+2}$	–	–
62.46 ± 0.39	$(4.41 \pm 0.69) \times 10^{+1}$	–	–	–
62.58 ± 0.39	–	–	$(2.10 \pm 0.19) \times 10^{+2}$	$(8.79 \pm 0.82) \times 10^{+1}$
62.68 ± 0.39	–	$(1.20 \pm 0.12) \times 10^{+2}$	–	–

Table 4: Measured cross sections for the production of Dy radionuclides in the irradiation of ^{nat}Tb with protons.

Proton energy (MeV)	Cross section (mb)			
	^{153}Dy	^{155}Dy	^{157}Dy	^{159}Dy
8.35 ± 2.53	–	–	–	$(6.45 \pm 0.46) \times 10^{+1}$
8.76 ± 2.45	–	–	–	$(7.73 \pm 0.55) \times 10^{+1}$
10.43 ± 2.22	–	–	–	$(1.01 \pm 0.07) \times 10^{+2}$
11.91 ± 2.06	–	–	–	$(9.10 \pm 0.64) \times 10^{+1}$
13.28 ± 1.94	–	–	–	$(7.16 \pm 0.51) \times 10^{+1}$
15.47 ± 1.78	–	–	$(1.17 \pm 0.11) \times 10^{+0}$	$(4.23 \pm 0.30) \times 10^{+1}$
17.45 ± 1.66	–	–	$(2.81 \pm 0.20) \times 10^{+1}$	$(2.89 \pm 0.21) \times 10^{+1}$
19.28 ± 1.56	–	–	$(1.63 \pm 0.11) \times 10^{+2}$	$(2.54 \pm 0.18) \times 10^{+1}$
20.98 ± 1.48	–	–	$(4.41 \pm 0.31) \times 10^{+2}$	$(2.36 \pm 0.17) \times 10^{+1}$
23.75 ± 1.37	–	–	$(8.47 \pm 0.59) \times 10^{+2}$	$(2.05 \pm 0.15) \times 10^{+1}$
26.89 ± 1.25	–	–	$(1.04 \pm 0.07) \times 10^{+3}$	$(1.90 \pm 0.14) \times 10^{+1}$
29.21 ± 1.17	–	–	$(9.70 \pm 0.68) \times 10^{+2}$	$(1.70 \pm 0.13) \times 10^{+1}$
31.41 ± 1.11	–	–	$(7.53 \pm 0.53) \times 10^{+2}$	$(1.57 \pm 0.11) \times 10^{+1}$
33.49 ± 1.04	–	–	$(5.23 \pm 0.37) \times 10^{+2}$	$(1.47 \pm 0.11) \times 10^{+1}$
35.48 ± 0.99	–	–	$(3.38 \pm 0.24) \times 10^{+2}$	$(1.32 \pm 0.09) \times 10^{+1}$
39.01 ± 0.89	–	$(3.90 \pm 0.28) \times 10^{+1}$	$(2.11 \pm 0.15) \times 10^{+2}$	$(1.31 \pm 0.09) \times 10^{+1}$
42.31 ± 0.81	–	$(2.16 \pm 0.15) \times 10^{+2}$	$(1.61 \pm 0.11) \times 10^{+2}$	$(1.18 \pm 0.09) \times 10^{+1}$
45.42 ± 0.74	–	$(4.29 \pm 0.30) \times 10^{+2}$	$(1.38 \pm 0.10) \times 10^{+2}$	$(1.13 \pm 0.08) \times 10^{+1}$
48.39 ± 0.67	–	$(5.19 \pm 0.36) \times 10^{+2}$	$(1.17 \pm 0.08) \times 10^{+2}$	$(1.05 \pm 0.08) \times 10^{+1}$
51.25 ± 0.61	–	$(5.06 \pm 0.35) \times 10^{+2}$	$(1.04 \pm 0.07) \times 10^{+2}$	$(1.00 \pm 0.07) \times 10^{+1}$
54.00 ± 0.55	–	$(4.75 \pm 0.33) \times 10^{+2}$	$(9.97 \pm 0.70) \times 10^{+1}$	$(9.65 \pm 0.80) \times 10^{+0}$
56.65 ± 0.50	–	$(3.75 \pm 0.26) \times 10^{+2}$	$(9.37 \pm 0.66) \times 10^{+1}$	$(8.86 \pm 0.72) \times 10^{+0}$
59.87 ± 0.44	$(6.97 \pm 0.71) \times 10^{+0}$	$(2.89 \pm 0.20) \times 10^{+2}$	$(9.15 \pm 0.64) \times 10^{+1}$	$(8.46 \pm 0.59) \times 10^{+0}$
62.97 ± 0.36	$(3.36 \pm 0.25) \times 10^{+1}$	$(2.14 \pm 0.15) \times 10^{+2}$	$(8.37 \pm 0.59) \times 10^{+1}$	$(8.14 \pm 0.66) \times 10^{+0}$
65.95 ± 0.30	$(7.75 \pm 0.55) \times 10^{+1}$	$(1.65 \pm 0.12) \times 10^{+2}$	$(7.45 \pm 0.52) \times 10^{+1}$	$(7.16 \pm 0.72) \times 10^{+0}$

Table 5: Measured cross sections for the production of Tb radionuclides in the irradiation of ^{nat}Tb with protons.

Proton energy (MeV)	Cross section (mb)			
	^{153}Tb	^{154m}Tb	^{155}Tb	^{156}Tb
23.75 ± 1.37	–	–	–	$(2.19 \pm 3.33) \times 10^{-1}$
26.89 ± 1.25	–	–	–	$(1.12 \pm 0.64) \times 10^{+0}$
29.21 ± 1.17	–	–	–	$(2.39 \pm 0.59) \times 10^{+0}$
31.41 ± 1.11	–	–	–	$(3.86 \pm 0.29) \times 10^{+0}$
33.49 ± 1.04	–	–	$(4.18 \pm 1.72) \times 10^{-1}$	$(7.46 \pm 0.54) \times 10^{+0}$
35.48 ± 0.99	–	–	$(1.27 \pm 0.21) \times 10^{+0}$	$(1.41 \pm 0.10) \times 10^{+1}$
39.01 ± 0.89	–	–	$(4.99 \pm 0.36) \times 10^{+1}$	$(4.11 \pm 0.29) \times 10^{+1}$
42.31 ± 0.81	–	–	$(2.61 \pm 0.18) \times 10^{+2}$	$(7.41 \pm 0.52) \times 10^{+1}$
45.42 ± 0.74	–	–	$(5.34 \pm 0.37) \times 10^{+2}$	$(1.05 \pm 0.07) \times 10^{+2}$
48.39 ± 0.67	–	–	$(6.63 \pm 0.46) \times 10^{+2}$	$(1.12 \pm 0.08) \times 10^{+2}$
51.25 ± 0.61	–	–	$(6.73 \pm 0.47) \times 10^{+2}$	$(1.14 \pm 0.08) \times 10^{+2}$
54.00 ± 0.55	$(3.08 \pm 1.59) \times 10^{-1}$	$(1.12 \pm 0.30) \times 10^{+0}$	$(6.65 \pm 0.47) \times 10^{+2}$	$(1.24 \pm 0.09) \times 10^{+2}$
56.65 ± 0.50	$(1.99 \pm 0.22) \times 10^{+0}$	$(1.41 \pm 0.18) \times 10^{+0}$	$(5.63 \pm 0.39) \times 10^{+2}$	$(1.23 \pm 0.09) \times 10^{+2}$
59.87 ± 0.44	$(1.38 \pm 0.10) \times 10^{+1}$	$(2.92 \pm 0.26) \times 10^{+0}$	$(4.71 \pm 0.33) \times 10^{+2}$	$(1.30 \pm 0.09) \times 10^{+2}$
62.97 ± 0.36	$(4.95 \pm 0.35) \times 10^{+1}$	$(4.99 \pm 0.51) \times 10^{+0}$	$(3.92 \pm 0.27) \times 10^{+2}$	$(1.23 \pm 0.09) \times 10^{+2}$
65.95 ± 0.30	$(1.14 \pm 0.08) \times 10^{+2}$	$(5.76 \pm 0.55) \times 10^{+0}$	$(3.30 \pm 0.23) \times 10^{+2}$	$(1.16 \pm 0.08) \times 10^{+2}$

Table 6: Measured cross sections for the production of Gd radionuclides in the irradiation of ^{nat}Tb with protons.

Proton energy (MeV)	Cross section (mb)	
	^{151}Gd	^{153}Gd
33.49 ± 1.17	–	$(2.36 \pm 0.22) \times 10^{-1}$
35.48 ± 1.11	–	$(9.67 \pm 0.70) \times 10^{-1}$
39.01 ± 1.04	–	$(4.57 \pm 0.32) \times 10^{+0}$
42.31 ± 0.99	–	$(8.80 \pm 0.62) \times 10^{+0}$
45.42 ± 0.89	–	$(1.17 \pm 0.08) \times 10^{+1}$
48.39 ± 0.81	–	$(1.44 \pm 0.10) \times 10^{+1}$
51.25 ± 0.74	–	$(8.92 \pm 0.63) \times 10^{+0}$
54.00 ± 0.68	$(9.06 \pm 1.14) \times 10^{-1}$	$(8.83 \pm 0.62) \times 10^{+0}$
56.65 ± 0.50	$(1.59 \pm 0.15) \times 10^{+0}$	$(8.34 \pm 0.56) \times 10^{+0}$
59.87 ± 0.46	$(5.71 \pm 0.41) \times 10^{+0}$	$(2.07 \pm 0.15) \times 10^{+1}$
62.97 ± 0.39	$(9.26 \pm 0.65) \times 10^{+0}$	$(3.98 \pm 0.28) \times 10^{+1}$
65.95 ± 0.30	$(1.11 \pm 0.08) \times 10^{+1}$	$(7.80 \pm 0.55) \times 10^{+1}$

Table 7: Production conditions for calculating the ^{155}Tb yield via ^{155}Dy decay in the proton bombardment of a thick ^{159}Tb target.

Production step	Duration (h)
Bombardment time	10.0
Waiting time 1	0.5
Chemical separation 1[a]	1.0
Waiting time 2	39.0
Chemical separation 2[b]	0.5
Waiting time 3	0.5

Exit proton energy: 35 MeV

Incident proton energy: Variable in range 50 - 70 MeV

[a] ^{155}Dy from ^{159}Tb target matrix

[b] ^{155}Tb from recovered ^{155}Dy

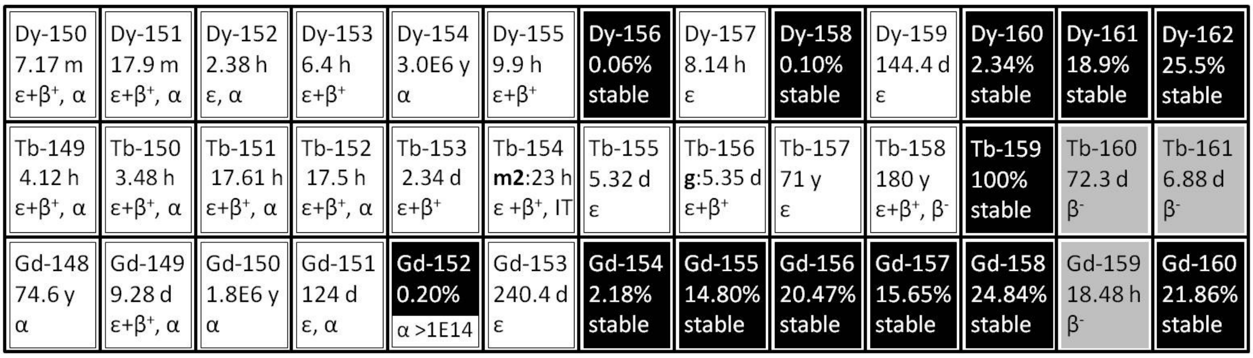

Dy-150 7.17 m $\varepsilon+\beta^+$, α	Dy-151 17.9 m $\varepsilon+\beta^+$, α	Dy-152 2.38 h ε, α	Dy-153 6.4 h $\varepsilon+\beta^+$	Dy-154 3.0E6 y α	Dy-155 9.9 h $\varepsilon+\beta^+$	Dy-156 0.06% stable	Dy-157 8.14 h ε	Dy-158 0.10% stable	Dy-159 144.4 d ε	Dy-160 2.34% stable	Dy-161 18.9% stable	Dy-162 25.5% stable
Tb-149 4.12 h $\varepsilon+\beta^+$, α	Tb-150 3.48 h $\varepsilon+\beta^+$, α	Tb-151 17.61 h $\varepsilon+\beta^+$, α	Tb-152 17.5 h $\varepsilon+\beta^+$, α	Tb-153 2.34 d $\varepsilon+\beta^+$	Tb-154 **m2**:23 h $\varepsilon+\beta^+$, IT	Tb-155 5.32 d ε	Tb-156 **g**:5.35 d $\varepsilon+\beta^+$	Tb-157 71 y ε	Tb-158 180 y $\varepsilon+\beta^+$, β^-	Tb-159 100% stable	Tb-160 72.3 d β^-	Tb-161 6.88 d β^-
Gd-148 74.6 y α	Gd-149 9.28 d $\varepsilon+\beta^+$, α	Gd-150 1.8E6 y α	Gd-151 124 d ε, α	Gd-152 0.20% α >1E14	Gd-153 240.4 d ε	Gd-154 2.18% stable	Gd-155 14.80% stable	Gd-156 20.47% stable	Gd-157 15.65% stable	Gd-158 24.84% stable	Gd-159 18.48 h β^-	Gd-160 21.86% stable

Figure 1: Simplified presentation of the relevant section of the nuclide chart containing data from Firestone & Eckström [8].

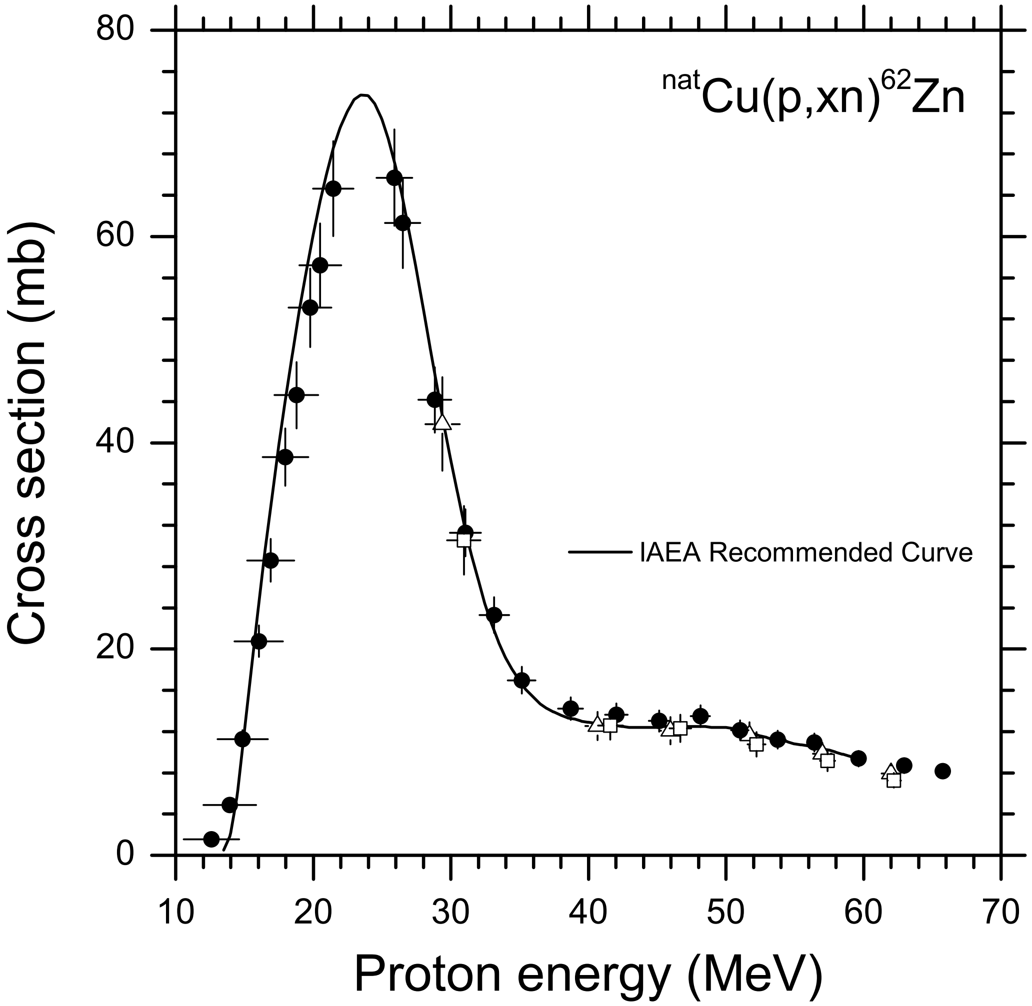

Figure 2: Monitor excitation function for the production of ^{62}Zn in the bombardment of ^{nat}Cu with protons. Open triangles: this work (Stack 1). Open squares: this work (Stack 2). Solid circles: this work (Stack 3 – see text for details).

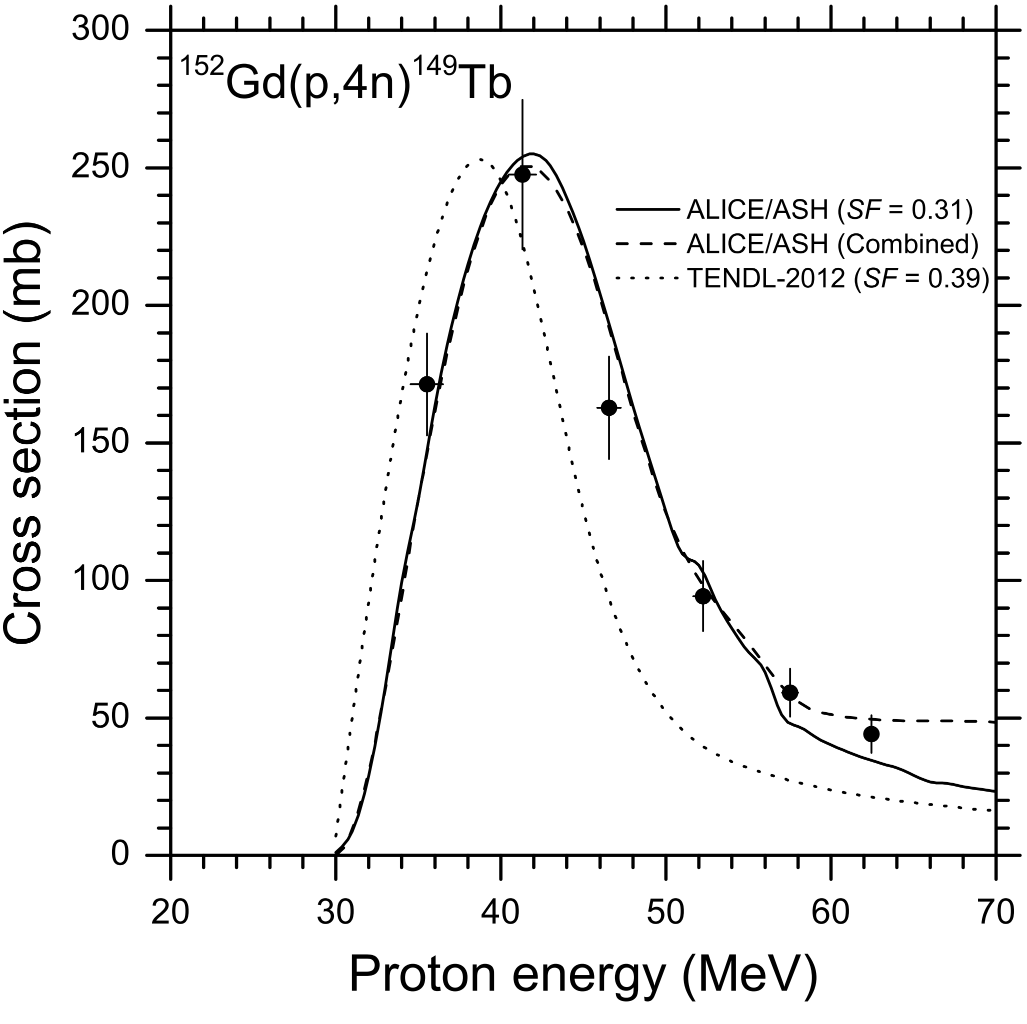

Figure 3: Excitation function for the production of ^{149}Tb in the irradiation of ^{152}Gd with protons. Solid circles: this work (Stack 1). The solid curve shows the results from ALICE/ASH calculations [18] and the dotted curve the corresponding values from the TENDL-2012 library [20, 21] for the (p,4n) reaction on ^{152}Gd only. The dashed curve also shows the ALICE/ASH calculations for the (p,4n) reaction with inclusion of co-produced contributions from the (p,6n) reaction on ^{154}Gd and the (p,7n) reaction on ^{155}Gd (see text). Note that the dashed curve has been lowered slightly relative to the solid curve to make it visible in the region of energy where the two curves overlap.

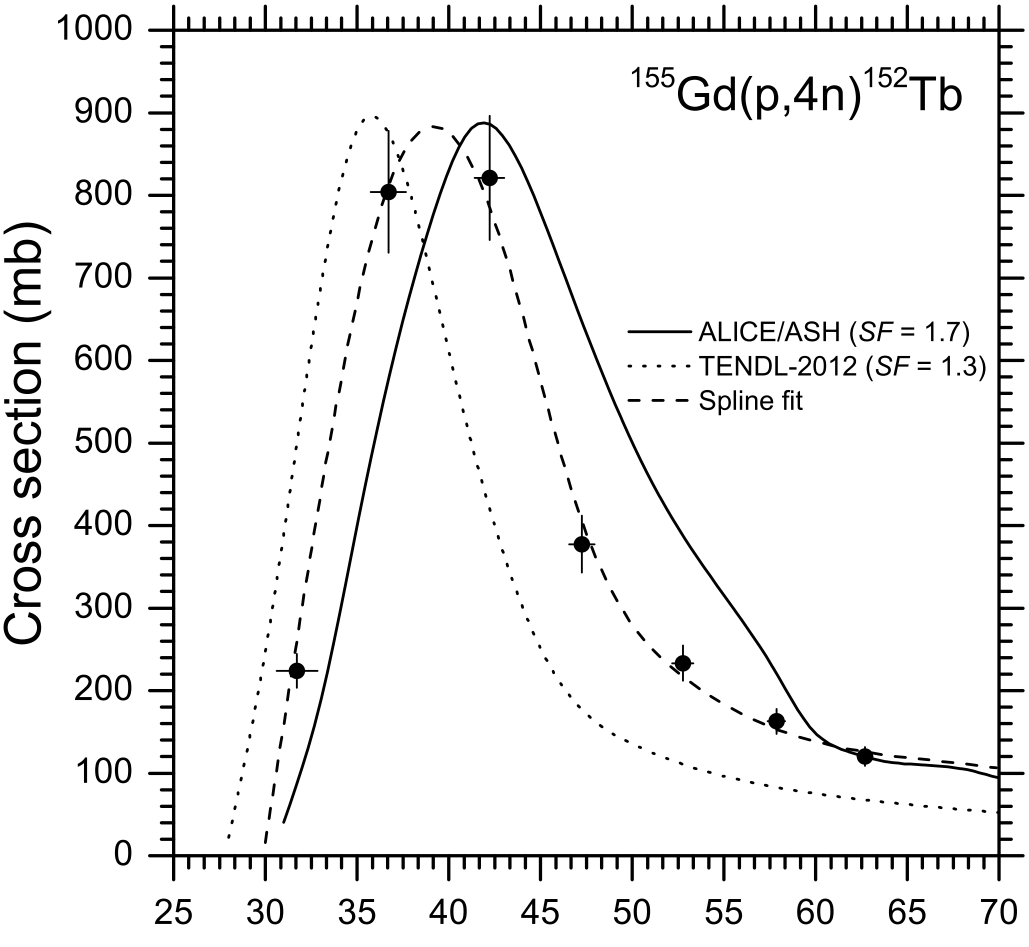

Figure 4: Excitation function for the production of ^{152}Tb in the irradiation of ^{155}Gd with protons. Solid circles: this work (Stack 2). See also caption to Fig. 3.

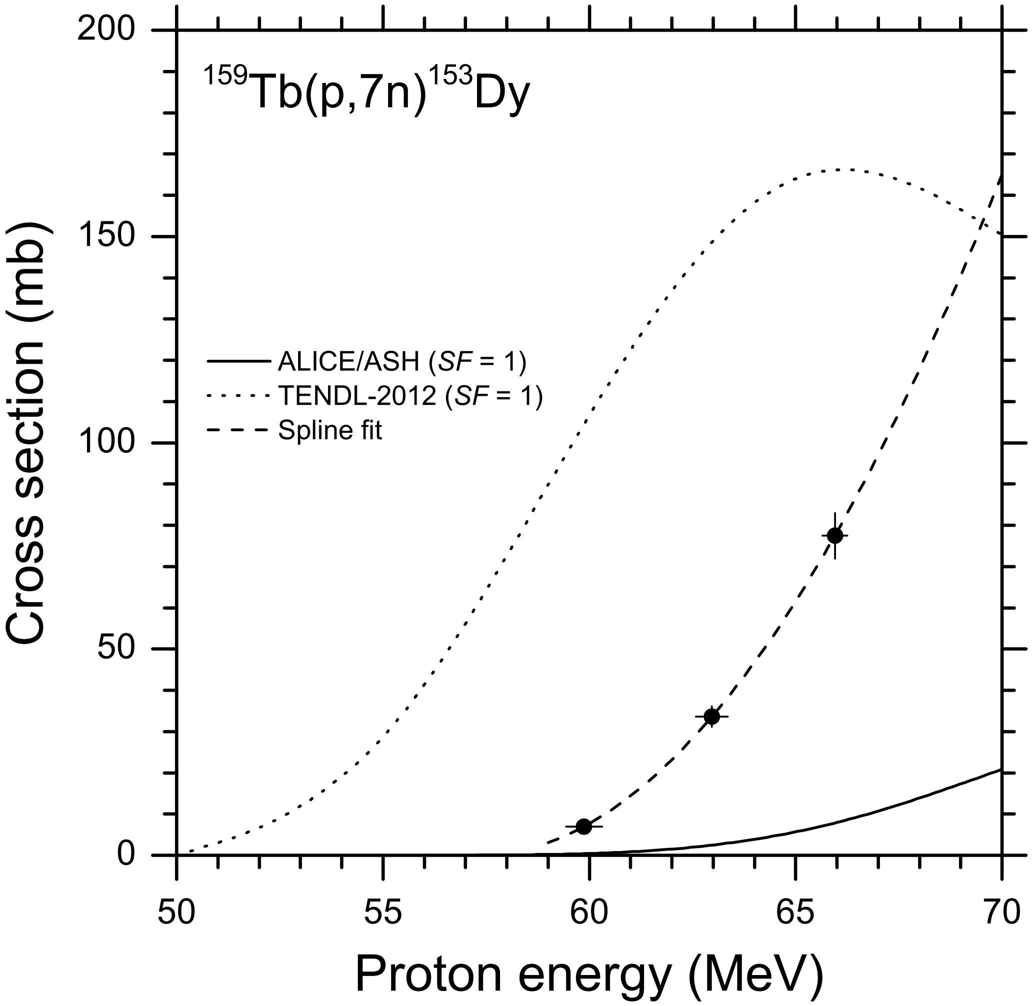

Figure 5: Excitation functions for the production of ^{153}Dy in the irradiation of ^{159}Tb with protons. Solid circles: this work (Stack 3). See also caption to Fig. 3.

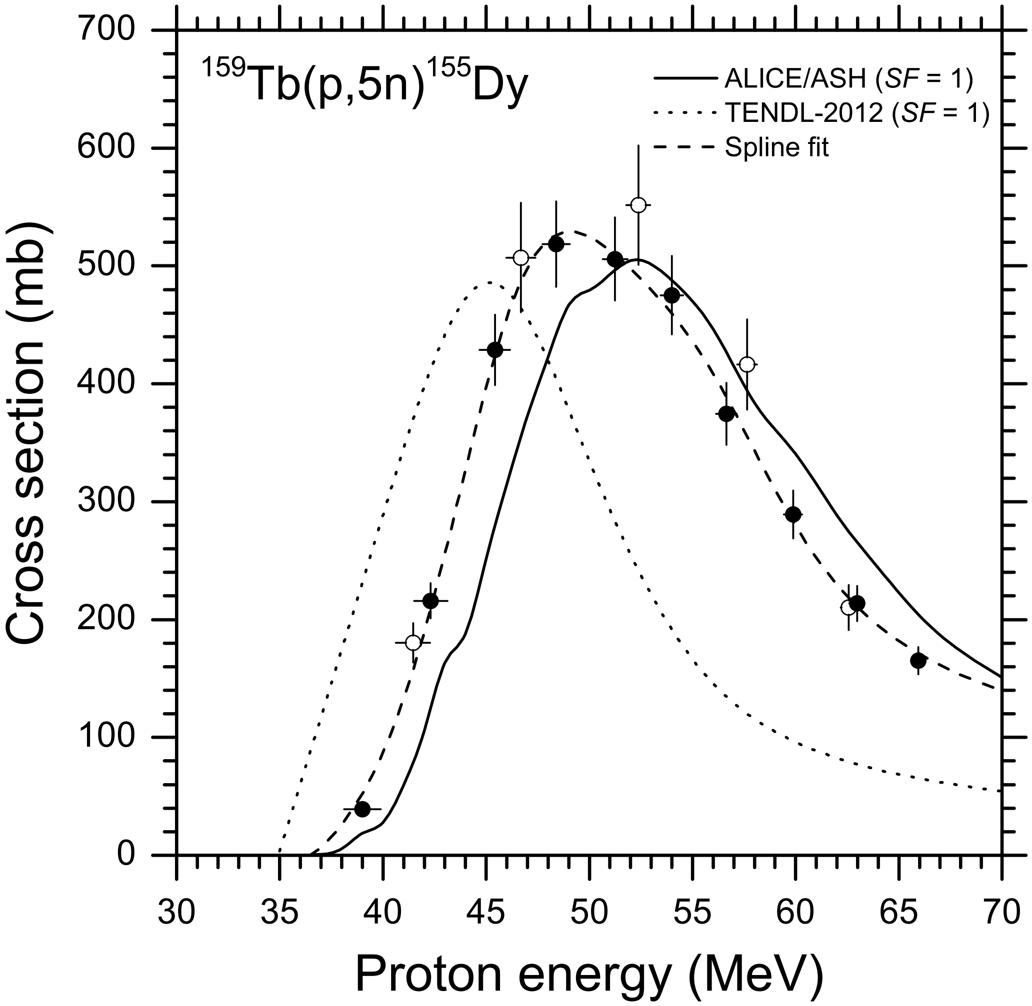

Figure 6: Excitation functions for the production of ^{155}Dy in the irradiation of ^{159}Tb with protons. Solid circles: this work (Stack 3). Open circles: this work (Stack 1). See also caption to Fig. 3.

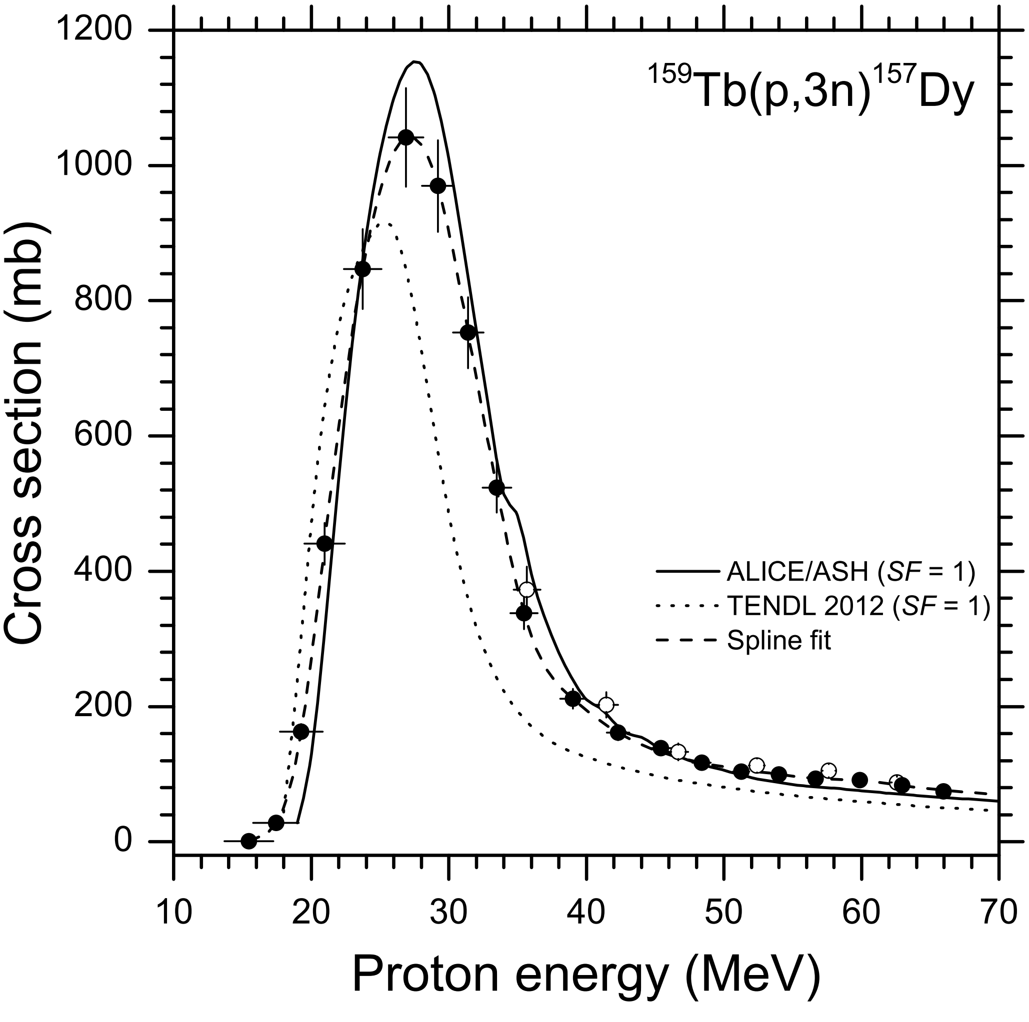

Figure 7: Excitation functions for the production of ^{157}Dy in the irradiation of ^{159}Tb with protons. Solid circles: this work (Stack 3). Open circles: this work (Stack 1). See also caption to Fig. 3.

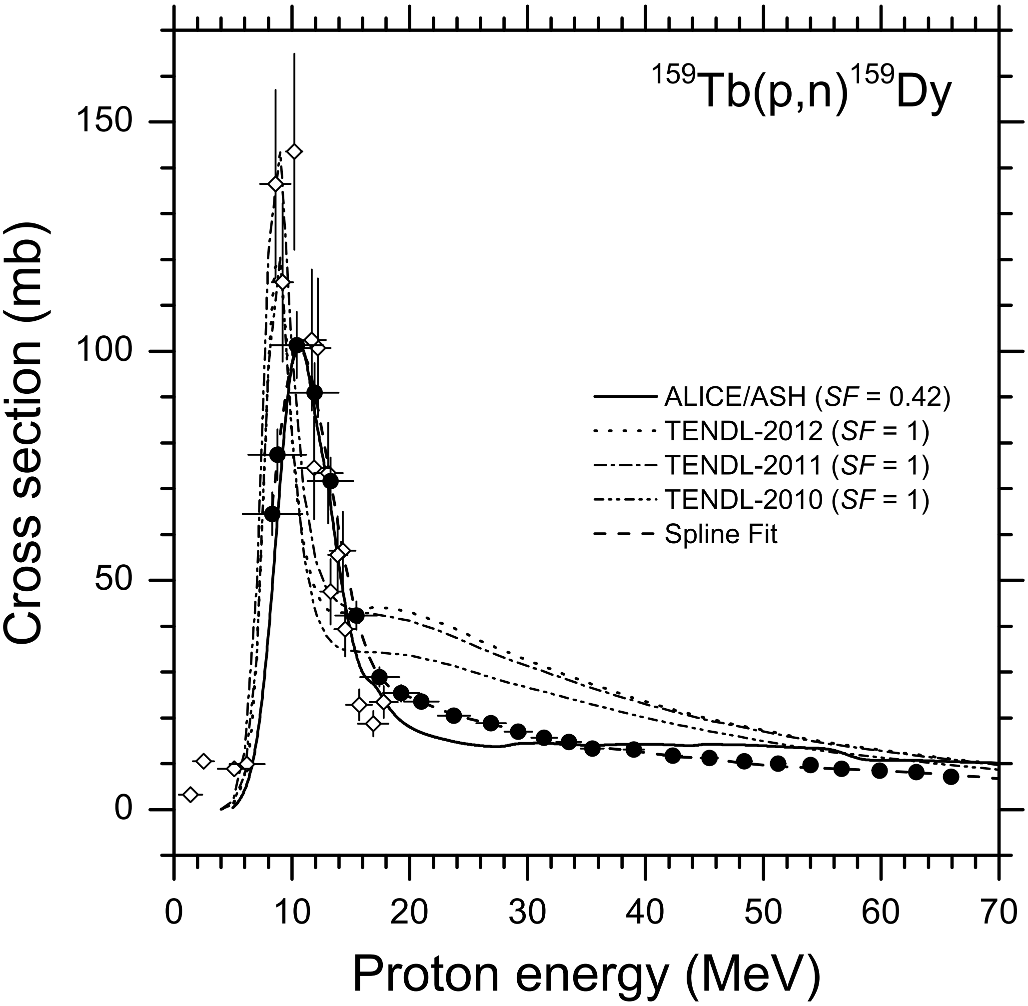

Figure 8: Excitation functions for the production of ^{159}Dy in the irradiation of ^{159}Tb with protons. Solid circles: this work (Stack 3). Open diamonds: Hassan *et al.* [22]. See also caption to Fig. 3.

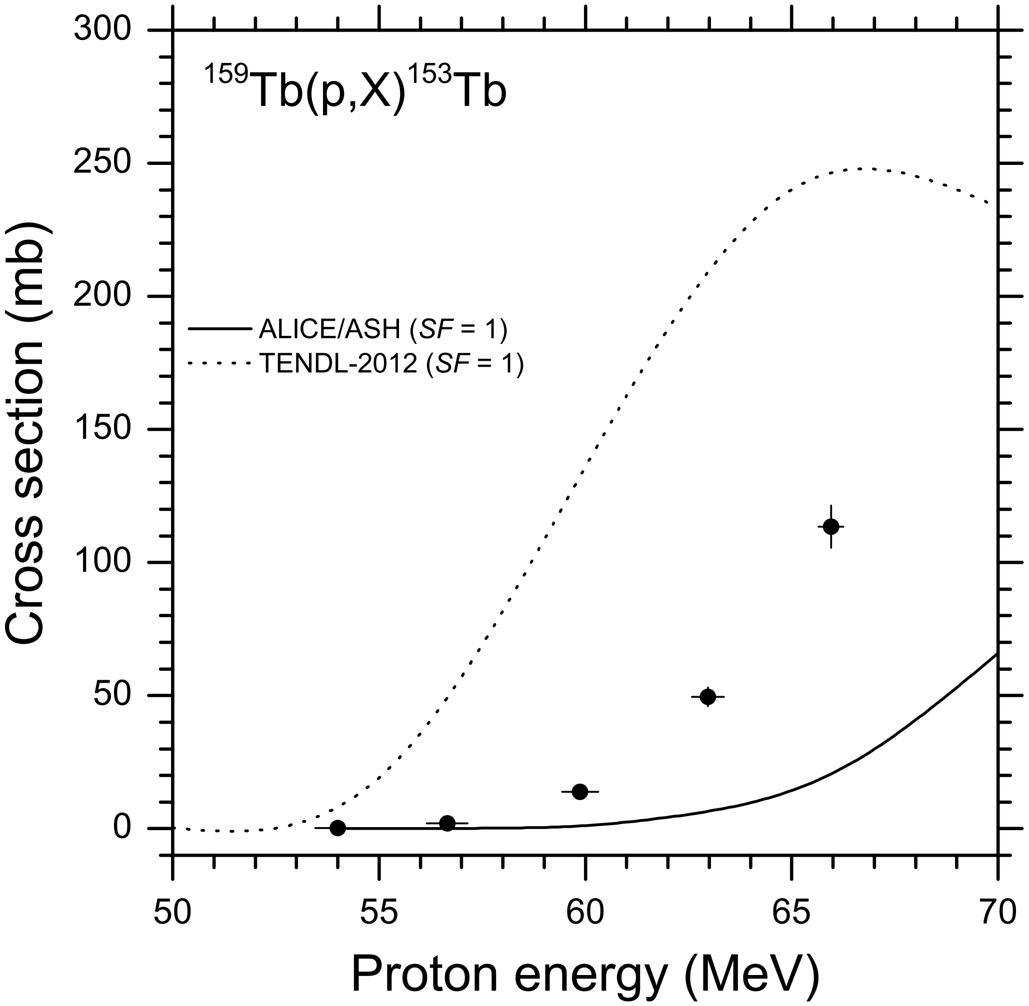

Figure 9: Excitation functions for the production of ^{153}Tb in the irradiation of ^{159}Tb with protons. Solid circles: this work (Stack 3). See also caption to Fig. 3.

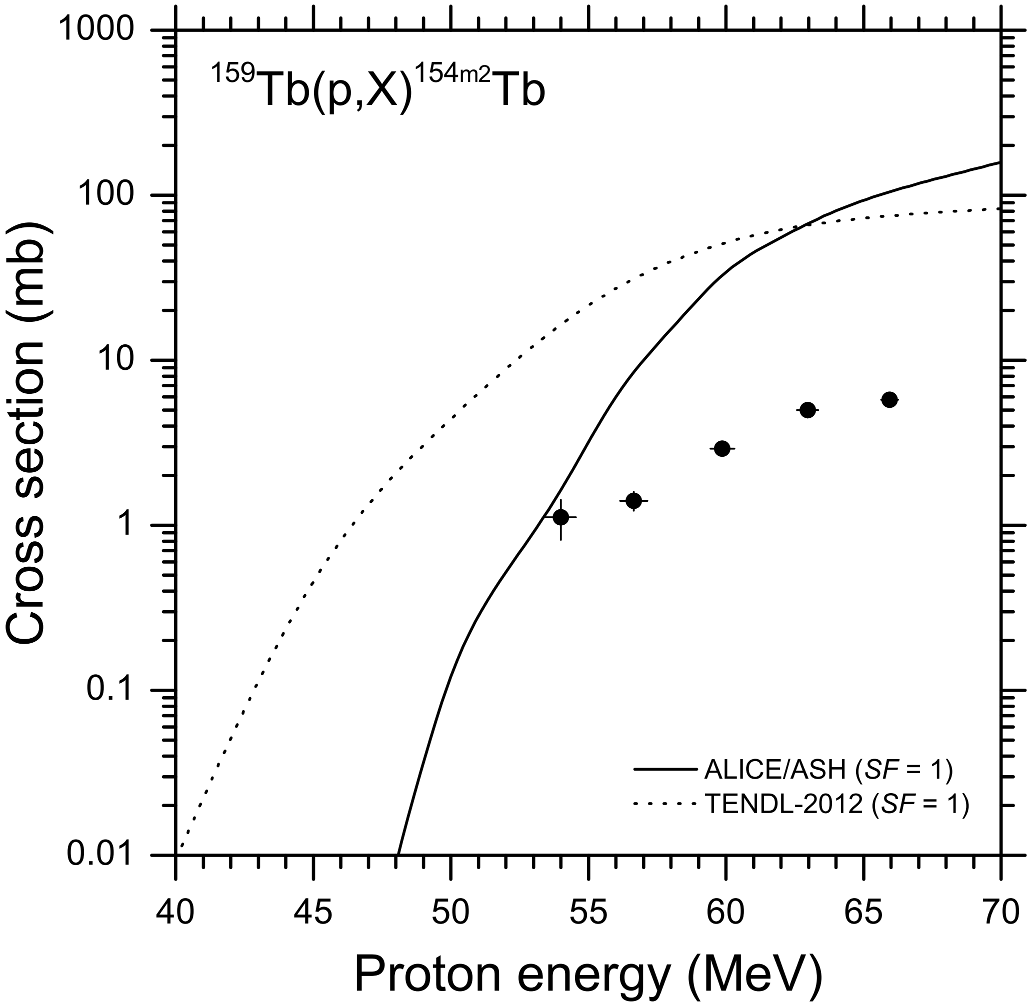

Figure 10: Excitation functions for the production of ^{154m2}Tb in the irradiation of ^{159}Tb with protons. Solid circles: this work (Stack 3). See also caption to Fig. 3.

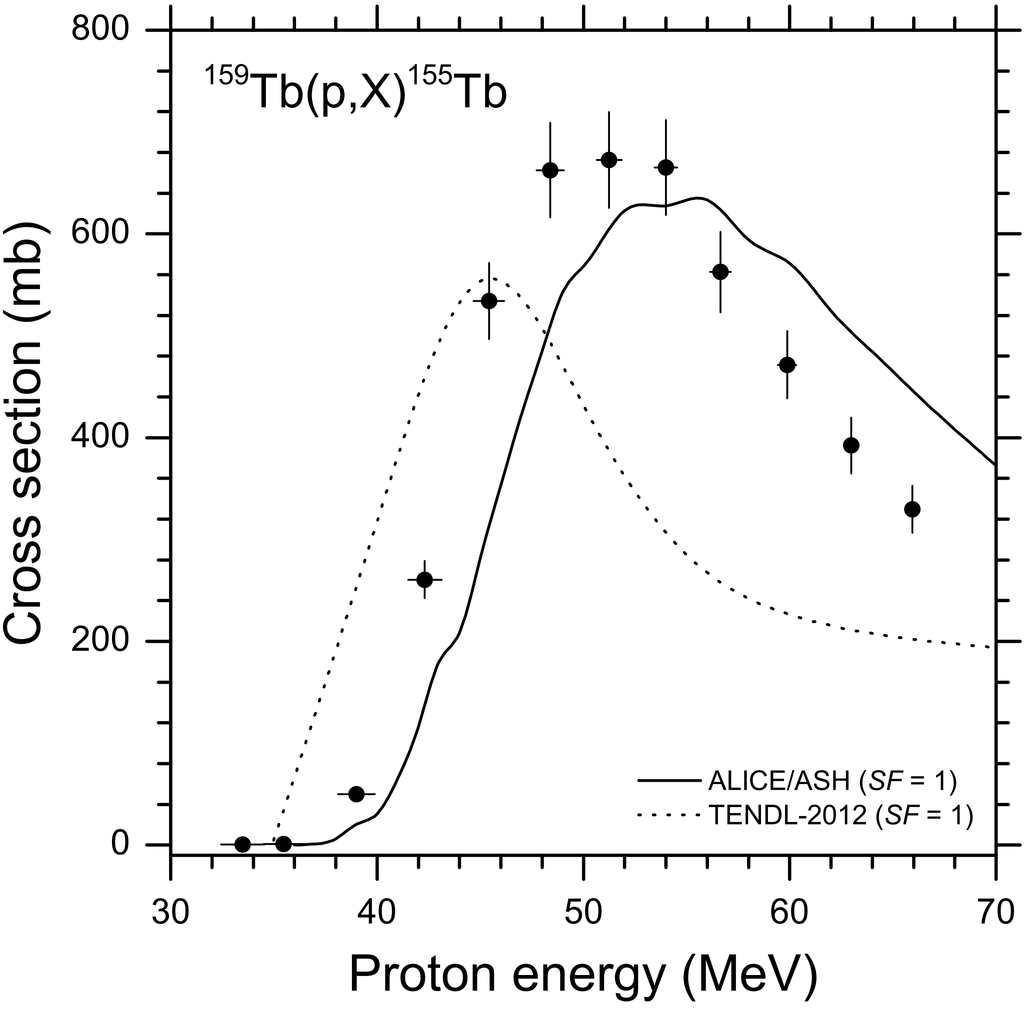

Figure 11: Excitation functions for the production of ^{155}Tb in the irradiation of ^{159}Tb with protons. Solid circles: this work (Stack 3). See also caption to Fig. 3.

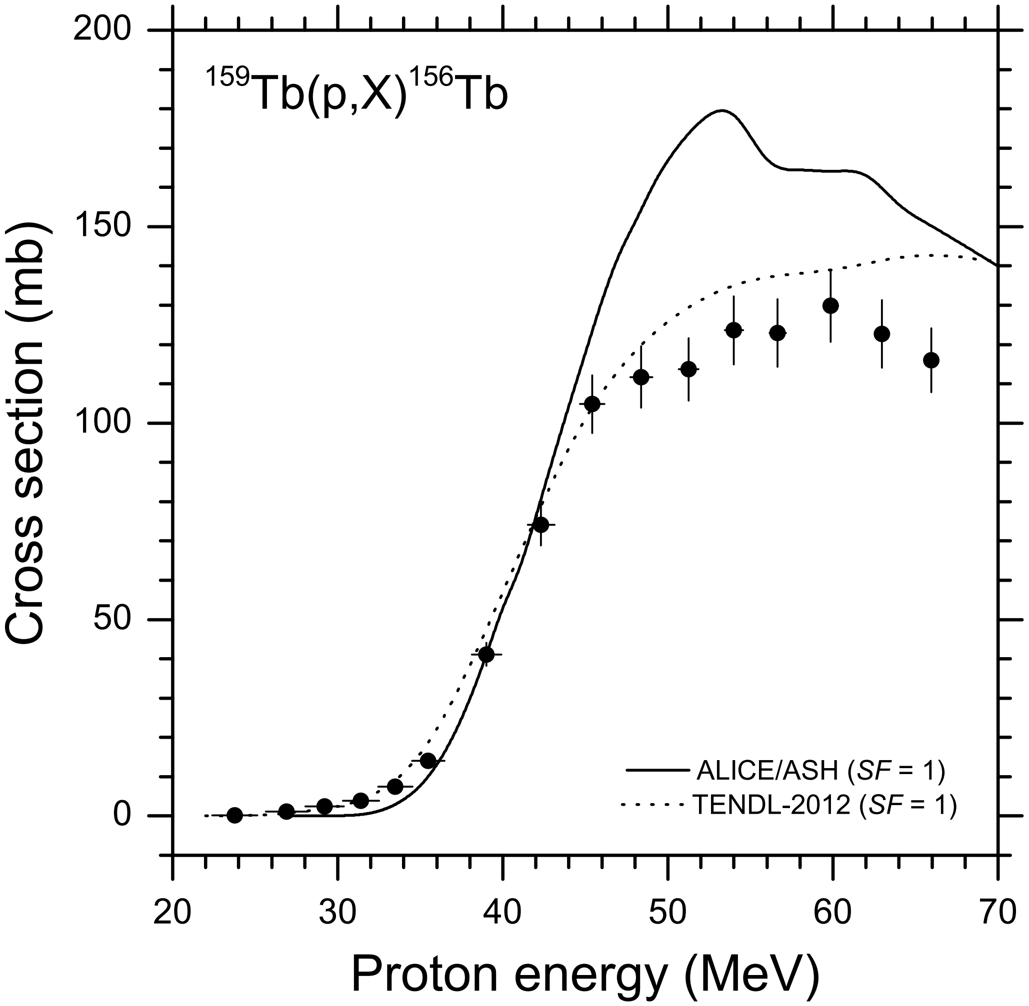

Figure 12: Excitation functions for the production of ^{156}Tb in the irradiation of ^{159}Tb with protons. Solid circles: this work (Stack 3). See also caption to Fig. 3.

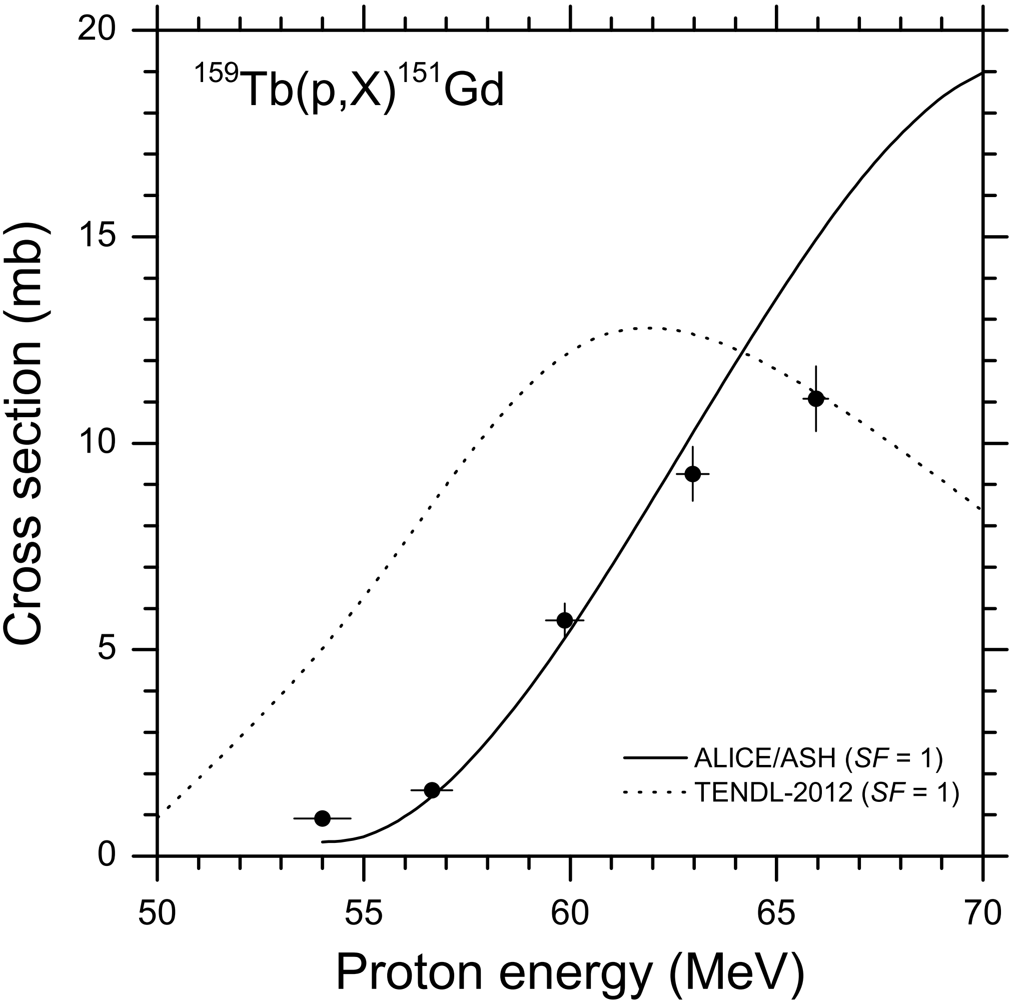

Figure 13: Excitation functions for the production of ^{151}Gd in the irradiation of ^{159}Tb with protons. Solid circles: this work (Stack 3). See also caption to Fig. 3.

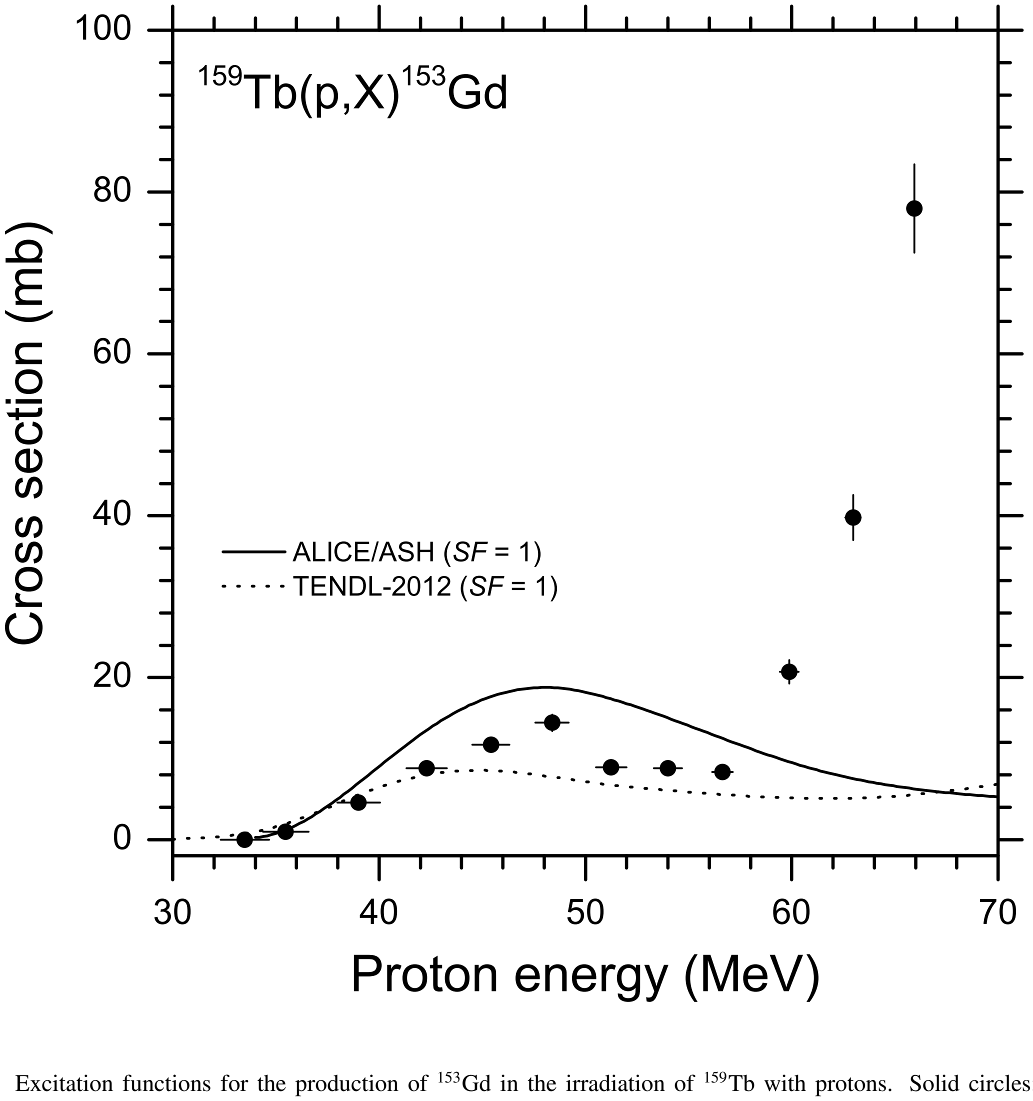

Figure 14: Excitation functions for the production of ^{153}Gd in the irradiation of ^{159}Tb with protons. Solid circles: this work (Stack 3). See also caption to Fig. 3.

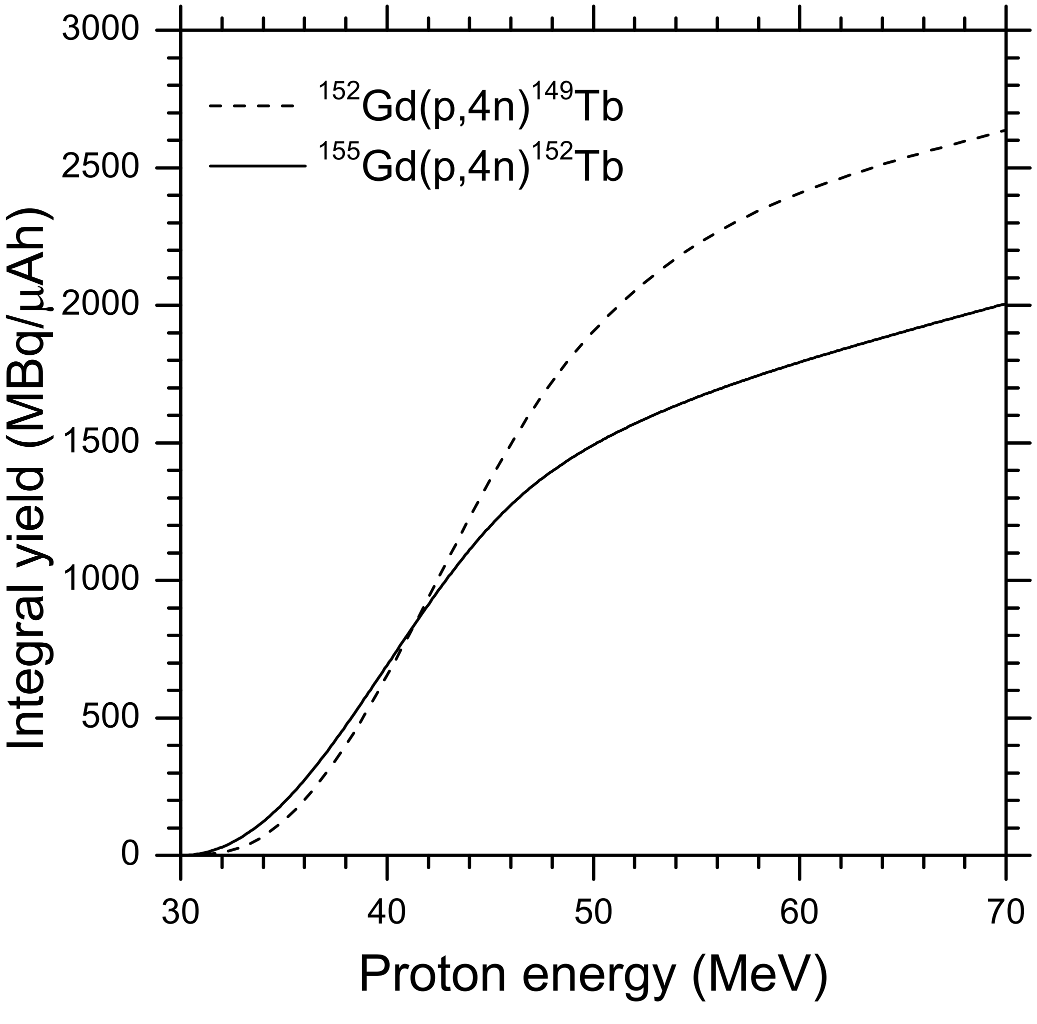

Figure 15: Integral physical yields for the production of ^{149}Tb and ^{152}Tb via (p,4n) reactions on targets of ^{152}Gd and ^{155}Gd, respectively. A 100% enrichment of the targets is assumed.

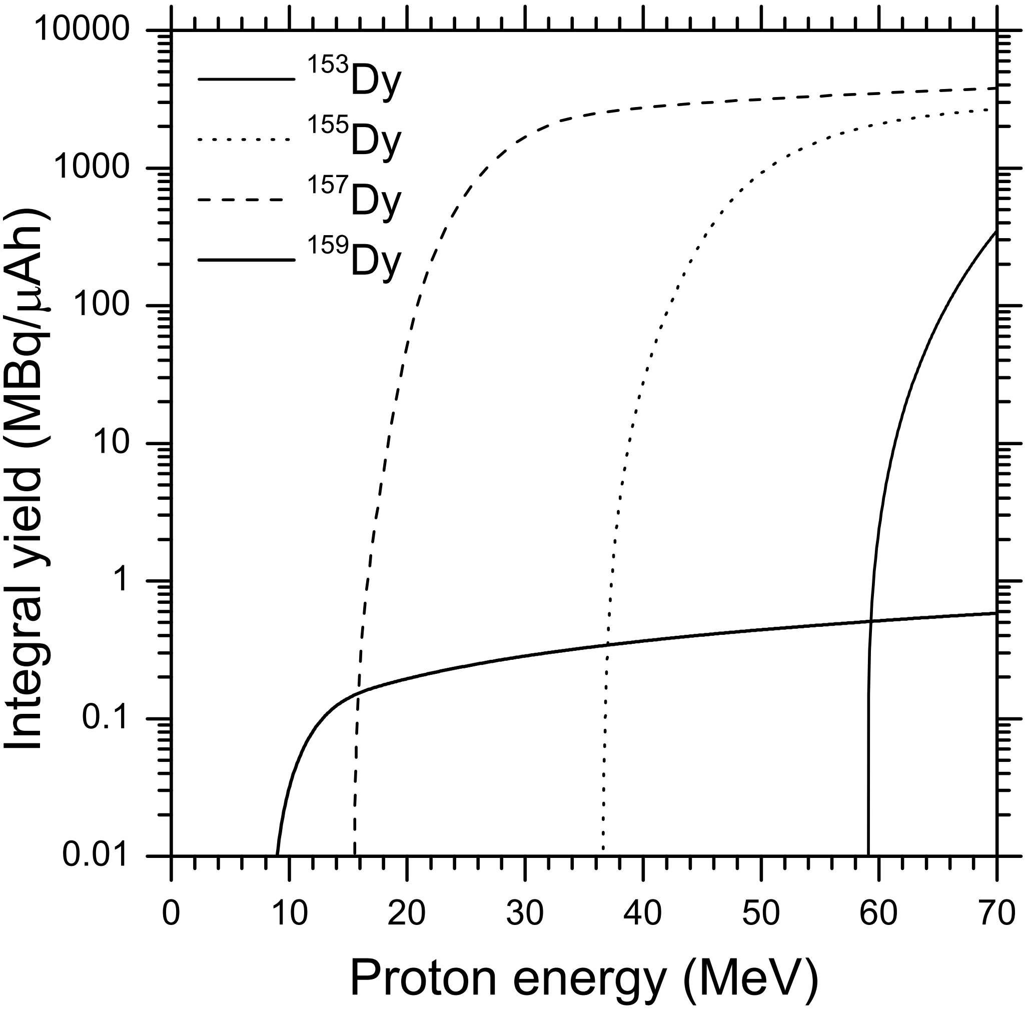

Figure 16: Integral physical yields for the production of ^{153,155,157,159}Dy in the proton bombardment of ^{159}Tb (natural Tb).

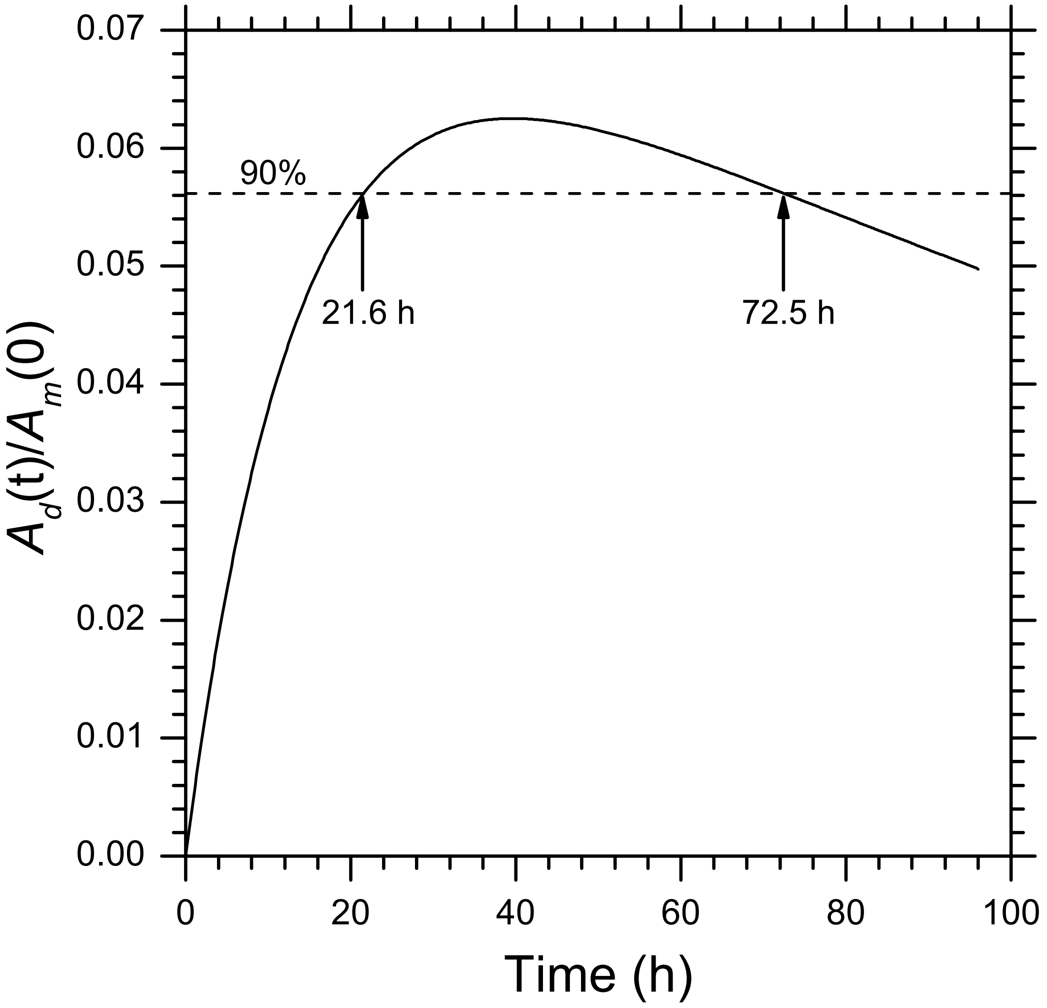

Figure 17: Growth and decay of ^{155}Tb formed in the decay of ^{155}Dy. A_d and A_m denote daughter and mother activities, respectively (see text).

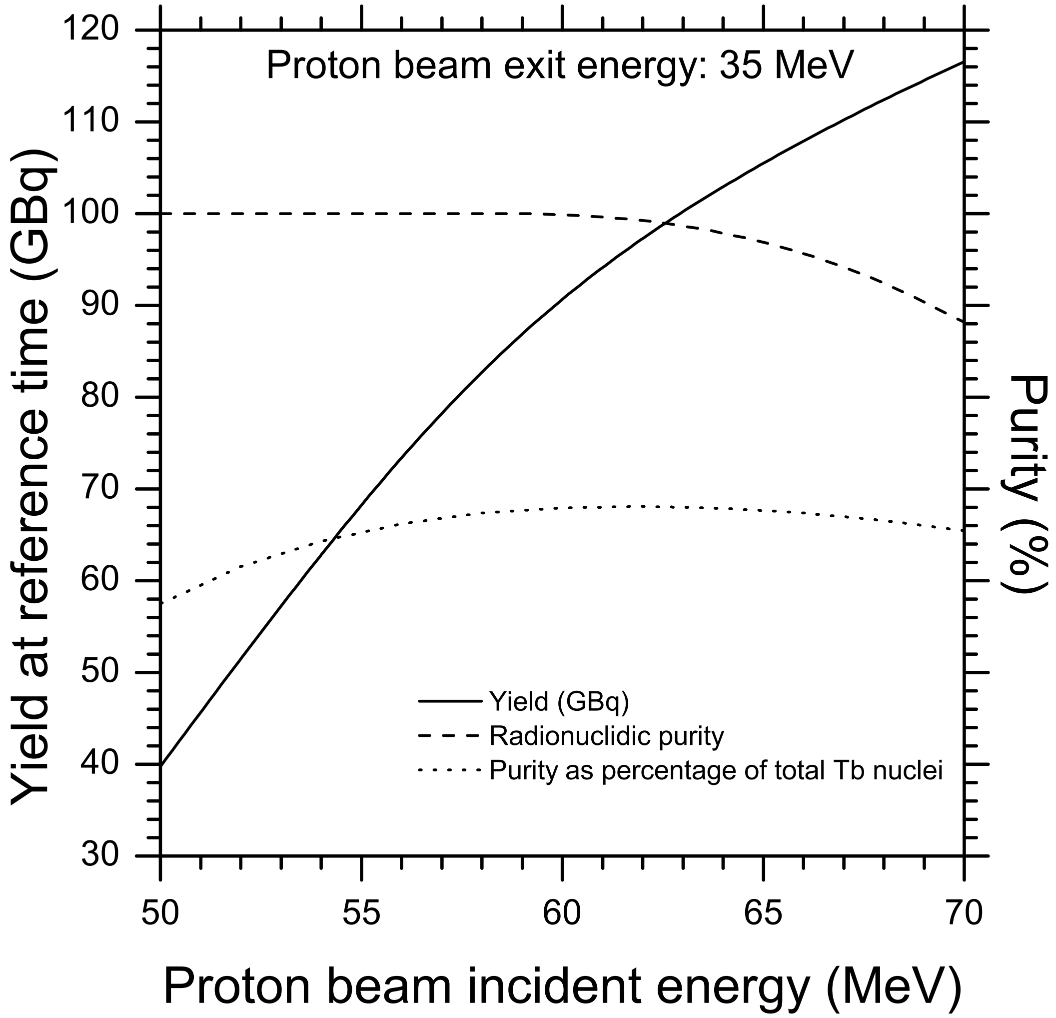

Figure 18: Production yield, radionuclidic purity as a percentage of total Tb radioactivity, and purity as a percentage of total Tb nuclei produced of ^{155}Tb in the proton bombardment of a thick Tb target, plotted as a function of incident beam energy. The exit proton energy is 35 MeV. The production conditions are those of Table 7.